A&A, 711, A104 (2026)
https://doi.org/10.1051/0004-6361/202658883

Astronomy & Astrophysics

Euclid: Discovery of 31 new quasars at $6.6 < z < 7.8$ ⋆

D. Yang[1,⋆⋆], J. F. Hennawi[1,2], F. Guarneri[3,4], J. Wolf[5], S. Belladitta[5,6], J.-T. Schindler[3], A. C. N. Hughes[7], E. Bañados[5], D. J. Mortlock[7,8], J. Yang[9], F. Wang[9], X. Fan[10], K. Jahnke[5], D. Stern[11], C. J. Willott[12], A. J. Barth[13], H. J. A. Rottgering[1], R. G. Varadaraj[14], R. Decarli[6], A.-C. Eilers[15,16], M. Ezziati[17], Y. Fu[1,18], J. Huang[2], X. Jin[9,19], Y. Kang[2], L. N. Martinez-Ramirez[5,20,21], Y. Matsuoka[22], M. Onoue[23,24], R. Pello[17], R. P. Remigio[13], W. L. Tee[25], B. Venemans[1], G. Vietri[26], B. Wang[27,1], L. J. Abbo[1], H. Atek[28], S. Bisogni[26], S. E. I. Bosman[29,5], R. A. A. Bowler[30], C. J. Conselice[30], F. B. Davies[5], C. M. Gutierrez[31,32], Y. Harikane[33], K. Rubinur[34], C. C. Lovell[35,36], M. Magliocchetti[37], J. Matthee[38], F. Ricci[39,40], M. Scialpi[41,42,43], D. Scott[44], L. Spinoglio[37], F. Tarsitano[45,46], Y. Toba[47,48], F. Walter[5], J. R. Weaver[16], G. Zamorani[6], B. Altieri[49], A. Amara[50], S. Andreon[51], H. Aussel[52], C. Baccigalupi[53,4,54,55], M. Baldi[56,6,57], A. Balestra[58], S. Bardelli[6], P. Battaglia[6], A. Biviano[4,53], E. Branchini[59,60,51], M. Brescia[61,62], S. Camera[63,64,65], G. Cañas-Herrera[66,1], V. Capobianco[65], C. Carbone[26], J. Carretero[67,68], M. Castellano[40], G. Castignani[6], S. Cavuoti[62,69], K. C. Chambers[70], A. Cimatti[71], C. Colodro-Conde[31], G. Congedo[66], L. Conversi[72,49], Y. Copin[73], F. Courbin[74,75,76], H. M. Courtois[77], M. Cropper[78], J.-C. Cuillandre[52], H. Degaudenzi[46], G. De Lucia[4], C. Dolding[78], H. Dole[79], M. Douspis[79], F. Dubath[46], X. Dupac[49], S. Dusini[80], S. Escoffier[81], M. Farina[37], R. Farinelli[6], S. Ferriol[73], F. Finelli[6,82], N. Fourmanoit[81], M. Frailis[4], E. Franceschi[6], M. Fumana[26], S. Galeotta[4], K. George[83], B. Gillis[66], C. Giocoli[6,57], P. Gómez-Alvarez[84,49], J. Gracia-Carpio[85], A. Grazian[58], F. Grupp[85,86], L. Guzzo[87,51,88], S. Gwyn[12], S. V. H. Haugan[34], H. Hoekstra[1], W. Holmes[11], I. M. Hook[89], F. Hormuth[90], A. Hornstrup[91,92], M. Jhabvala[93], S. Kermiche[81], B. Kubik[73], K. Kuijken[1], M. Kümmel[86], M. Kunz[94], H. Kurki-Suonio[95,96], A. M. C. Le Brun[97], S. Ligori[65], P. B. Lilje[34], V. Lindholm[95,96], I. Lloro[98], G. Mainetti[99], D. Maino[87,26,88], E. Maiorano[6], O. Mansutti[4], O. Marggraf[100], M. Martinelli[40,101], N. Martinet[17], F. Marulli[102,6,57], R. J. Massey[103], H. J. McCracken[28], E. Medinaceli[6], S. Mei[104,105], Y. Mellier[106,28], M. Meneghetti[6,57], E. Merlin[40], G. Meylan[107], J. J. Mohr[83], A. Mora[108], M. Moresco[102,6], L. Moscardini[102,6,57], E. Munari[4,53], R. Nakajima[100], C. Neissner[109,68], R. C. Nichol[50], S.-M. Niemi[110], C. Padilla[109], S. Paltani[46], F. Pasian[4], K. Pedersen[111], W. J. Percival[112,113,114], V. Pettorino[110], S. Pires[52], G. Polenta[115], M. Poncet[116], L. A. Popa[117], L. Pozzetti[6], G. D. Racca[110,1], F. Raison[85], R. Rebolo[31,118,32], A. Renzi[119,80], J. Rhodes[11], G. Riccio[62], H.-W. Rix[5], E. Romelli[4], M. Roncarelli[6], C. Rosset[104], B. Rusholme[120], R. Saglia[86,85], Z. Sakr[29,121,122], D. Sapone[123], M. Sauvage[52], M. Schirmer[5], P. Schneider[100], T. Schrabback[124], A. Secroun[81], G. Seidel[5], S. Serrano[125,126,127], E. Sihvola[128], P. Simon[100], C. Sirignano[119,80], G. Sirri[57], L. Stanco[80], J. Steinwagner[85], P. Tallada-Crespí[67,68], I. Tereno[129,130], N. Tessore[78], S. Toft[131,132], R. Toledo-Moreo[133], F. Torradeflot[68,67], I. Tutusaus[127,125,121], L. Valenziano[6,82], J. Valiviita[95,96], T. Vassallo[4], Y. Wang[120], J. Weller[86,85], F. M. Zerbi[51], E. Zucca[6], G. Fabbian[79], M. Huertas-Company[31,134,135], J. Martín-Fleitas[136], P. Monaco[137,4,54,53], V. Scottez[106,138], and M. Viel[53,4,55,54,139]

(Affiliations can be found after the references)

Received 7 January 2026 / Accepted 28 April 2026

ABSTRACT

We report the discovery of 31 new high-z quasars in the redshift range $6.6 < z < 7.8$. These quasars were selected from approximately 3000 deg^2 of sky covered during the first 1.5 years of the Euclid Wide Survey, representing the initial results of the *Euclid* high-z quasar search. Our candidate selection employed multiple machine-learning and probabilistic techniques applied to the *Euclid* $I_{\rm E}$, $Y_{\rm E}$, $J_{\rm E}$, and $H_{\rm E}$ images, supplemented by ancillary z-band data when available. Spectroscopic follow-up observations were carried out with Keck, Magellan, and the Large Binocular Telescope (LBT). Among the new discoveries, there are 12 quasars at $z \geq 7$, more than doubling the number of previously known quasars at $z \geq 7$. The newly discovered quasars exhibit $21.2 < J_{\rm E} < 23.2$ ($-25.5 < M_{1450} < -23.6$), extending quasar studies to the faint end of the quasar luminosity function (QLF) at $z \gtrsim 7$. The quasar with the highest-z, EUCL J172902.75+641018.1 at $z \approx 7.77$, sets the new redshift record for the most distant quasar ever reported. These discoveries demonstrate *Euclid*'s transformative role in high-z quasar discovery and set the stage for future follow-up studies of the early galaxies hosting quasars, supermassive black hole growth, and the intergalactic medium in the epoch of reionisation.

Key words. galaxies: active – galaxies: high-redshift – quasars: general – quasars: supermassive black holes – dark ages, reionization, first stars

⋆ This paper is published on behalf of the Euclid Consortium.

⋆⋆ Corresponding author: dyang@strw.leidenuniv.nl

1. Introduction

Since the first discovery of quasars at $z > 5.7$ (corresponding to <1 Gyr of cosmic time assuming a ΛCDM model; Fan et al. 2000), subsequent searches over the past two decades have pushed the redshift frontier to $z \sim 7.5$, and have provided key insights into galaxy formation and cosmology (for a review see Fan et al. 2023). Specifically, the highest-redshift quasars ($z \gtrsim 7.5$; Bañados et al. 2018; Yang et al. 2020a; Wang et al. 2021) place stringent constraints on the formation and growth of supermassive black holes (SMBHs): only the most massive black hole seeds appear to be sufficient to produce these quasars within the limited cosmic time available under the standard Eddington-limited accretion scenario (e.g., Inayoshi et al. 2020; Yang et al. 2021; Farina et al. 2022; Bosman et al. 2025). Beyond this, submillimetre observations of some other high-z quasars indicate that their host galaxies might be among the most massive ($>10^{10}\,M_{\odot}$; e.g., Neeleman et al. 2021) and actively star-forming (star-formation rate above $100\,M_{\odot}\,\mathrm{yr}^{-1}$; e.g., Wang et al. 2024) objects known in the early Universe. At the same time, the SMBHs powering these luminous quasars appear to be overmassive relative to the local SMBH-galaxy mass relation (e.g., Kormendy & Ho 2013), suggesting an early SMBH-galaxy coevolution scenario, in which black hole growth outpaces that of the host galaxy (e.g. Neeleman et al. 2021; Farina et al. 2022; Yue et al. 2024; Wang et al. 2024; but also see Lauer et al. 2007; Izumi et al. 2019; Li et al. 2022; Silverman et al. 2025). Finally, as the most luminous non-transient sources in the Universe, high-z quasars serve as powerful beacons for studying the intergalactic medium (IGM), the reionisation (e.g., Davies et al. 2018; Yang et al. 2020b; Greig et al. 2024; Kist et al. 2025; Hennawi et al. 2025) and large-scale structure (LSS) during the epoch of reionisation (EoR; e.g., Wang et al. 2023; Pizzati et al. 2024; Eilers et al. 2024).

However, a major challenge to fully understanding high-z quasars and leveraging them as probes of the early Universe is our limited knowledge of the quasar population at $z > 7$. Prior to this work, only nine quasars were found at $z > 7$ since the first discovery in 2011 (Mortlock et al. 2011; Bañados et al. 2018; Wang et al. 2018; Matsuoka et al. 2019a,b; Yang et al. 2020a; Wang et al. 2021; Bañados et al. 2025b; Matsuoka et al. 2025), while hundreds of quasars had been identified at $6 < z < 7$. The lack of large samples at $z > 7$ hinders us from tracing the evolutionary pathways of the quasars towards their formation and from constraining the IGM and LSS at earlier epochs. While the time interval between $z = 7$ and $z = 6$ spans only of the order of 200 Myr, key astrophysical processes can evolve significantly over such timescales. SMBHs, for instance, can grow rapidly under Eddington-limited accretion, which corresponds to an e-folding (Salpeter) timescale of ∼45 Myr assuming a fiducial radiative efficiency of 10%, allowing their masses to increase by a factor of ∼100 within this period. Concurrently, the IGM is expected to undergo drastic evolution, with the neutral hydrogen fraction changing from nearly unity at $z \gtrsim 7$ to $\lesssim 1\%$ at $z \sim 5.5$ (e.g., Planck Collaboration VI 2020; Bosman et al. 2022; Jin et al. 2023; Davies et al. 2026).

Despite the critical importance of extending the analyses of quasars to $z \gtrsim 7$, finding them remains exceptionally challenging. Quasars at this epoch are among the rarest objects in the Universe, with a typical surface density of approximately 1 per $100\,\mathrm{deg}^2$ down to $J = 23$ (e.g., Matsuoka et al. 2023). Moreover, at $z \gtrsim 7$ the Lyα transition is redshifted to $\gtrsim 1\,\mu$m, which happens to match both the band gap energy at which silicon-based CCDs become insensitive, and where atmospheric OH emission significantly elevates the sky background. Thus, assembling a large sample at $z \gtrsim 7$ requires deep large area near-infrared (NIR) imaging surveys–a task that remains prohibitively difficult from the ground.

In February 2024, the *Euclid* telescope (1.2 m; Euclid Collaboration: Mellier et al. 2025) commenced the six-year Euclid Wide Survey (EWS; Euclid Collaboration: Scaramella et al. 2022), which aims at mapping $14\,000\,\mathrm{deg}^2$ of the extragalactic sky. At the core of the mission are two instruments, the Visible Camera (VIS; Euclid Collaboration: Cropper et al. 2025) and the Near Infrared Spectrometer and Photometer (NISP; Euclid Collaboration: Jahnke et al. 2025), which observe the sky simultaneously in the optical and NIR using a dichroic beamsplitter. *Euclid* achieves unprecedented depths for a wide-field survey in both optical and NIR, reaching 5σ limits of 24.5 in the NIR and 26.2 in the optical for point sources. For comparison, the UKIRT Infrared Deep Sky Survey (UKIDSS; Lawrence et al. 2007) and the VISTA Kilo-degree Infrared Galaxy (VIKING) Survey (Edge et al. 2013) cover $\sim 1000\,\mathrm{deg}^2$ and reach $\lesssim 22$ mag in the NIR; the VISTA Hemisphere Survey (VHS; McMahon et al. 2013) covers $\sim 20\,000\,\mathrm{deg}^2$ and reaches ∼21 mag in its J band; and the UKIRT Hemisphere Survey (UHS; Dye et al. 2018) covers $\sim 10\,500\,\mathrm{deg}^2$ and reaches ∼20.5 mag in its J band. The unprecedented survey area and depth of *Euclid* make it a game-changer for the field of high-z quasar searches.

Euclid Collaboration: Barnett et al. (2019) predicted the discovery of over 100 quasars with $7.0 < z < 7.5$, and ∼25 quasars beyond $z = 7.5$, including an order of 8 beyond $z = 8.0$ from the full EWS. These predicted detections extend into the regime of faint quasars ($J \sim 23$) at $z \gtrsim 7$, comparable to those identified in the deepest ground-based surveys; namely, the Subaru High-z Exploration of Low-Luminosity Quasars (SHELLQs; e.g., Matsuoka et al. 2016) and the Canada–France High-z Quasar Survey (CFHQS; e.g., Willott et al. 2010), but over vastly larger sky coverage and at significantly higher redshifts.

This paper presents the initial results of the *Euclid* high-z quasar search using the on-the-fly data of the EWS (see Sect. 2.3) between 14 February and 11 August 2025. The imaging data and photometric catalogues used for the candidate selection are introduced in Sect. 2, followed by a brief overview of the candidate selection methods in Sect. 3. The spectroscopic follow-up observation of these candidates are described in Sect. 4. The new quasar discoveries are presented and discussed in Sect. 5. When relevant, we adopt the following cosmological parameters: $\Omega_{\mathrm{m}} = 0.3111$, $\Omega_{\Lambda} = 0.6899$, $\Omega_{\mathrm{b}} = 0.0489$, $h = 0.6766$, and $\sigma_8 = 0.8102$ (Planck Collaboration VI 2020). All the magnitudes are presented in the AB system (Oke & Gunn 1983).

2. EWS and photometry catalogues

2.1. EWS

As introduced in Sect. 1, the EWS, conducted from 2024 to 2030, is designed to map approximately $14\,000\,\mathrm{deg}^2$ of the extragalactic sky in both visible and NIR bands using the two onboard instruments: VIS and NISP. The survey employs a step-and-stare observing strategy, in which the spacecraft collects data at fixed sky positions before slewing to subsequent pointings. Each pointing covers a field of view of $0.53\,\mathrm{deg}^2$, with VIS and NISP operating simultaneously. Observations at each field are performed using a four-point dither pattern. The EWS reaches 5σ point-source sensitivities of 24.5 mag in the three NIR bands, Y_{E}

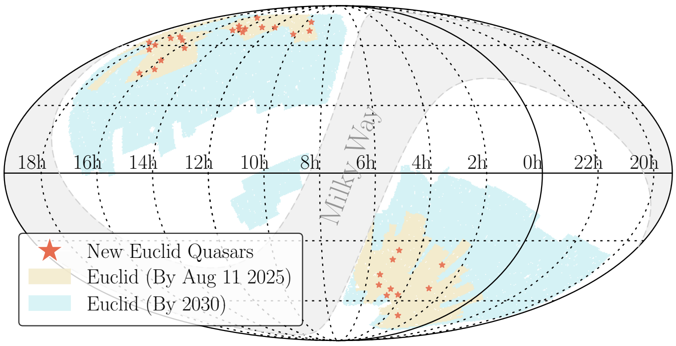

Fig. 1. Projection of the EWS area and the locations of the newly discovered quasars in J2000.0 equatorial coordinates. The regions observed by 11 August 2025, utilised for the quasar search presented in this work, are shown in beige. The full survey footprint expected by the end of the mission in 2030 is overlaid in cyan. The positions of newly discovered *Euclid* high-z quasars are marked in red.

(949.6–1212.3 nm), J_{E} (1167.6–1567.0 nm), and H_{E} (1521.5–2021.4 nm), and 26.2 mag in the broad optical band I_{E} (550–900 nm). NISP also provides grism slitless spectroscopy across the full EWS, with a resolving power of $R > 480$ over the range 1206–1892 nm (Euclid Collaboration: Schirmer et al. 2022) for a point source. Although this work uses only *Euclid*'s photometry, the spectroscopy has strong potential for the direct identification of luminous high-z quasars (see Bañados et al. 2025a). However, the grism data are relatively shallow and will detect only the brightest quasars.

The quasar search described in this work utilised EWS imaging data acquired between 14 February 2024 and 11 August 2025, as shown in Fig. 1. The total area covered amounts to approximately 3000 deg^2, with roughly 1040 deg^2 located in the northern hemisphere and 1960 deg^2 in the southern hemisphere. We note that the ground-based spectroscopic follow-up observations over these regions, particularly in the south, is ongoing and has not yet reached full completeness. A comprehensive statistical analysis of the selection function and the quasar population will be presented in forthcoming publications.

2.2. Ancillary imaging surveys

While *Euclid* imaging provides the primary basis for our quasar candidate selection, ancillary data from external surveys are also incorporated to enhance selection efficiency and robustness. Specifically, as the I_{E} band is a broad optical filter, deep z-band imaging can significantly improve the ability to detect the IGM absorption trough and to select robust high-z quasar candidates at $z \gtrsim 7$. To this end, we performed forced photometry on z-band images obtained with the Hyper Suprime-Cam (HSC; Miyazaki et al. 2018) as part of the Ultraviolet Near-Infrared Optical Northern Survey (UNIONS; Gwyn et al. 2025), or from the Dark Energy Survey (DES; Dark Energy Survey Collaboration 2016) when available. The 5σ depth of these z-band images are 24.1 (2″ diameter aperture) and 23.1 (1.″95 diameter aperture), respectively. These images are processed through the *Euclid* Processing Function `EXT` (see Sect. 2.3 for details).

Additionally, we make use of the LOFAR Two-metre Sky Survey (LoTSS; Shimwell et al. 2022) to prioritise candidates with associated radio emission (e.g., Gloudemans et al. 2022). We specifically utilise data from LoTSS Data Release 3, which covers ≈89% of the northern sky at a central frequency of 144 MHz, with a median rms sensitivity of ∼100 µJy beam^{-1} and beam size of 6″.

2.3. Related Euclid processing functions and data products

The Euclid Consortium (EC) has developed a suite of software Processing Functions (PFs) to efficiently manage and process the vast volume of data generated by *Euclid*. This study utilises image and catalogue products produced at various processing levels by several of these PFs, namely `VIS`, `NIR`, `MER`, and `EXT`. In this subsection, we provide a brief overview of the relevant data products.

`VIS`. The `VIS` PF generates calibrated optical images and source catalogues from raw *Euclid* VIS exposures. It includes a calibration pipeline for instrumental corrections and a science pipeline for applying the corrections and conducting measurements. Multiple dithered exposures are co-added using `SWarp` (Bertin 2010) to produce stacked images, from which PSF models are derived with `PSFEx` (Bertin 2013) and source catalogues are extracted using `SExtractor` (Bertin & Arnouts 1996). The most relevant `VIS` data products to this work are the stacked images and their associated catalogues. More details about `VIS` PF are given in Euclid Collaboration: McCracken et al. (2026).

`NIR`. The `NIR` PF processes raw NISP exposures to produce calibrated NIR images and catalogues. It includes a common pre-processing stage shared with the spectroscopic pipeline, calibration, and stacking components. Stacked images are generated from dithered exposures per field, accompanied by PSF models computed with `PSFEx`, and source catalogues extracted using `SExtractor`. For this work, we primarily use these stacked NIR images and catalogues in the Y_{E}, J_{E}, and H_{E} bands. For more details about the `NIR` PF, we refer the readers to Euclid Collaboration: Polenta et al. (2026).

`MER`. The `MER` PF constructs multi-wavelength photometric catalogues by merging calibrated imaging data from the `VIS` and `NIR` PFs with external ground-based data (e.g. UNIONS). It produces background-subtracted mosaics per band and performs independent source detection on stacked VIS images and on a combined NIR detection image. The resulting catalogues include multi-band photometry (Kron, aperture, and template-fitting), morphological classifications, and quality flags. Photometric measurements are computed using PSF-matched images and convolution kernels. The input PSFs from `NIR`/`VIS` were propagated for each mosaiced image and evaluated at the detected source positions, together with the PSF convolution kernels. For the southern sky, instead of using `NIR`/`VIS` stacked frames, we used the `MER` mosaics to perform photometry measurements (see Sect. 3.1). For more details, we refer to Euclid Collaboration: Romelli et al. (2026).

`EXT`. The `EXT` PF ingests and calibrates external ground-based imaging data for integration with *Euclid* data products. In principle, `EXT` images (e.g. z band) are already incorporated into `MER`. However, in cases where the external data were available but `MER` had not yet been triggered, due to the incomplete coverage of certain external bands, we directly utilised the calibrated `EXT` single-epoch frames for forced-photometry measurements.

After raw data from the spacecraft were downlinked, they were processed within the Euclid Data Processing System (DPS), where all data products are generated and tracked through successive PFs. Once validated, these data are pushed to the Science Archive System (SAS) in its on-the-fly (OTF) environment. The data in DPS and OTF are processed soon after acquisition to provide access as early as possible. As a result, different PF versions may be used, and the processing is therefore heterogeneous. The publicly available data are distributed through the SAS Public Data Release environment, where all products are reprocessed homogeneously using a fixed set of PFs. The data used in this work were taken directly from the DPS, and are thus not part of any data release. The motivation is to access the largest possible sky area before each follow-up confirmation campaign to search for extremely rare objects.

3. Photometric candidate selection

3.1. Custom photometry catalogues for candidate selection

The candidate selection was initiated based on available *Euclid* catalogues to create custom PSF photometry catalogues that fully exploit the sensitivity of *Euclid* for point-like sources. With the PSF photometry, we assessed the probability of each candidate being a quasar with multiple algorithms described in Sect. 3.2. Specifically, we first selected optically faint, point-like sources from the `VIS+NIR` catalogues and then performed PSF photometry on this pre-selected sample. Two parallel workflows were employed for the photometric measurements, depending on the availability of `MER` products at the time of data processing and spectroscopic follow-up. When `MER` products were not yet available, fluxes in the *Euclid* bands were measured directly on the `VIS` and `NIR` stacked images. In this case, z-band fluxes were obtained by averaging the measurement from individual single-epoch frames delivered by the `EXT` PF (see Sect. 2.3). When `MER` mosaics were available, all fluxes – including those in the *Euclid* and external bands – were measured directly from the co-added `MER` images. A more detailed summary of the workflow is as follow:

Step 1 – Cross-matching sources across the three NISP bands using a $0\farcs3$ matching radius to build a combined NIR source catalogue from the single-band `SExtractor` catalogues created by `NIR`.

Step 2 – Applying signal-to-noise ratio (S/N) cuts in the $J_{\rm E}$ and $H_{\rm E}$ bands (S/N $>$ 5), and select isolated sources by requiring the angular distance to the nearest NIR-detected neighbour to exceed $1\farcs2$.

Step 3 – Selecting point-like sources by requiring the `SExtractor` parameter `CLASS_STAR` > 0.6 in both the $J_{\rm E}$ and $H_{\rm E}$ bands.

Step 4 – Identifying all VIS observations overlapping with the given NISP observation.

Step 5 – For each overlapping VIS pointing, cross-matching the cleaned NIR source catalogue with the corresponding VIS catalogue using a $0\farcs3$ radius. Select dropout candidates by identifying sources with no VIS detection or with faint VIS flux relative to their $J_{\rm E}$ flux ($f_{I_{\rm E}}/f_{J_{\rm E}} < 0.06$, equivalent to $I_{\rm E} - J_{\rm E} > 3.05$).

Step 6 – Discarding sources whose image in VIS is affected by pixel-masking or segmentation, to ensure reliable flux measurements.

Step 7 – Measuring the PSF fluxes in each band, including the z band when available, using `Photutils` (Bradley et al. 2016). The local background is estimated from an annular region using a 3σ-clipped statistic. As noted previously, when `MER` products are available, fluxes are measured from the `MER` mosaics; otherwise, they are extracted from the `VIS` and `NIR` stacked images. All three PFs construct PSF models with `PSFEx` (Bertin 2013) on a per-tile or per-pointing basis. For the `VIS` and `NIR` stacks, we use the average PSF stamp, while for the `MER` mosaics, we adopted the PSF stamp closest to each target.

Step 8 – Defining the final dropout sample by applying the colour selection criteria on the PSF fluxes: $f_{I_{\rm E}}/f_{J_{\rm E}} < 0.06$ (equivalent to $I_{\rm E} - J_{\rm E} > 3.05$) and $|f_z/f_{J_{\rm E}}| < 2$ (equivalent to $z - J_{\rm E} > 0.75$).

These catalogues were subsequently passed to the candidate selection pipeline to produce the final targets list.

3.2. Selection algorithms

Our candidate selection method employed several different algorithms to enhance the efficiency and robustness. Candidates were independently selected from the photometric catalogues introduced in Sect. 3.1 using these algorithms. Each method provides both a photometric redshift estimate ($z_{\rm phot}$) and a quantitative selection metric. Empirical thresholds on these metrics were applied to select high-confidence candidates from each method. Artefacts and spurious sources were subsequently removed through a visual inspection. Candidates were manually prioritised during spectroscopic follow-up, taking into account the outputs from all three methods. This process resulted in a final, merged list of high-priority targets. Detailed descriptions of the implementation of each algorithm and assessments of their performance will be presented in forthcoming publications. Here, we provide a brief overview of the methodologies.

The first method, Extreme Deconvolution High-Redshift Quasar selection (XDHZQSO) is based on the framework introduced and implemented in Nanni et al. (2022) and Yang et al. (2024), but adopts conditional density estimation (Kang et al. 2025) so that the densities of different populations vary smoothly with additional variables. Specifically, we consider only two classes, high-z quasar and an all-inclusive contaminant class. We model their densities in flux-ratio space (relative to $J_{\rm E}$) using the Extreme Deconvolution technique (Bovy et al. 2011), allowing the means and covariances of the Gaussian mixture to vary continuously depending on $J_{\rm E}$ magnitude and, for quasars, redshift. The quasar density is built from synthetic photometry generated with a new generative model (D. Yang et al., in prep.), trained on a sample of 16 198 quasars within the redshift range $0.45 < z < 3.0$, drawn from the SDSS-III BOSS and the SDSS-IV Extended BOSS (eBOSS) surveys (Dawson et al. 2013, 2016). The contaminant density is estimated empirically from the flux-ratio distribution of the pre-selected sources described in Sect. 3.1, which are overwhelmingly non-quasar contaminants. This approximation is justified because contaminants outnumber true high-z quasars by several orders of magnitude in this sample.

The second method employs XGBoost (Chen & Guestrin 2016), a widely adopted gradient-boosting algorithm for selecting quasars in large photometric catalogues (e.g., Calderone et al. 2024; Fu et al. 2025). This second approach uses the same two-class formulation as the first method, considering only a high-z quasar population and an all-inclusive contaminant population. Using fluxes and flux ratios as features, we construct a training set with positive and negative examples. We generated positives via an independent, machine learning-based model (Guarneri et al. 2026) trained on the same SDSS III and SDSS IV BOSS/eBOSS quasar set as above; negatives are drawn from the full pre-selected dataset. The classifier returns a per-source probability, $P_{\rm QSO}$, used to vet the candidate list by removing all sources with $P_{\rm QSO} < P_{\rm QSO,th} = 0.85$ and prioritise high-probability objects. A second XGBoost model is then trained via quantile regression and only on positive examples to estimate photometric redshifts and their associated uncertainties.

Our third method uses template-based SED fitting with `eazypy` (Brammer et al. 2008) and `LePhare` (Arnouts & Ilbert

2011). Both codes are supplied with the same custom template library, which is based on the extragalactic template sets of Salvato et al. (2022) and Wolf et al. (2024), and extended to include common stellar contaminants (Martínez-Ramírez et al. 2026). For every object we compute the statistic $R_{\chi^2} \equiv \chi^2_\star / \chi^2_{\rm gal}$, where $\chi^2_\star$ and $\chi^2_{\rm gal}$ denote the best-fit χ^2 values for the stellar and extragalactic template families, respectively. Objects with $R_{\chi^2} > 3$ were retained and ordered by decreasing R_{χ^2}.

Finally, following Mortlock et al. (2012), Euclid Collaboration: Barnett et al. (2019), and Ezziati et al. (2025), we implemented a Bayesian model comparison (BMC) procedure. We constructed colour models for high-z quasars and the principal contaminants (MLT dwarfs and intermediate-redshift galaxies). For each source, we evaluated the class-conditional likelihoods that explicitly account for photometric uncertainties, assumed to be Gaussian-distributed. These likelihoods are combined with analytic surface-density priors that depend on redshift, apparent magnitude, and Galactic coordinates to yield the posterior quasar probability P_q. Candidates were then ranked by P_q and we retained those with $P_q \geq 0.5$.

4. Spectroscopic follow-up observation

To confirm the high-z quasar candidates, spectroscopic observations with large-aperture telescopes were essential. We conducted the follow-up campaign using the Keck I and Keck II telescopes (10 m) at the W. M. Keck Observatory, the Magellan Baade telescope (6.5 m) at Las Campanas Observatory, and the LBT on Mount Graham. Spectroscopic follow-up was conducted over 20.5 nights across the 2024A, 2024B, 2025A, and 2025B semesters. Six different instruments were employed to confirm the new quasars reported in this work: the Low Resolution Imaging Spectrometer (LRIS; Oke et al. 1995) and the Multi-Object Spectrometer For Infra-Red Exploration (MOSFIRE; McLean et al. 2012) on Keck I, the Keck Cosmic Web Imager (KCWI; Morrissey et al. 2018; McGurk et al. 2024) on Keck II, the Folded-port InfraRed Echellette (FIRE; Simcoe et al. 2010) on the Magellan Baade telescope, the Multi-object Double Spectrograph (MODS; Pogge et al. 2010) and the LBT Utility Camera in the Infrared (LUCI; Seifert et al. 2003) on LBT. A summary of the discovery observations obtained with these instruments is presented in Table A.1. Detailed descriptions of the instruments and the associated observations are provided in the following sub-sections.

4.1. Keck/LRIS

LRIS is an optical double spectrograph on Keck I. For the purpose of high-z quasar confirmation, we only used the red channel with a plate scale of 0.″123 per pixel. For this program, we used a 1″ slit, the gold-coated 600/10 000 grating, and the D680 dichroic. The data were binned over 2 × 2 pixels before readout. This configuration provided a wavelength coverage of 750–1060 nm and a spectral resolution of full width at half maximum (FWHM) ∼ 150 kms^{-1} ($R \sim 2000$). Each observing sequence consisted of four 300 s exposures, and each target was typically observed through one to three such sequences.

Observations were carried out in the 2024A semester (U259, PI: Hennawi), with a total of 2.5 nights allocated, split into five half-nights in June and July 2024. One half-night of observation was cancelled due to extreme weather conditions on the summit. The seeing was around 0.″8–1″ during the remaining time.

4.2. Keck/KCWI

KCWI is an optical integral field spectrograph mounted on Keck II. For this program, we only used the red-channel, namely the Keck Cosmic Reionization Mapper (KCRM; McGurk et al. 2024). Observations were conducted using the medium slicer configuration, which provides a field of view of 16.″5 × 20.″4, composed of 24 slices each with a slice width of 0.″69. The RM2 grating was employed in the red arm, covering 894–1070 nm. A binning of 2 × 2 was applied. The spectral resolution of this setup is FWHM ≈ 107 kms^{-1} ($R \sim 2800$). Like our LRIS program, each observing sequence also included four 300 s exposures, and each target was typically observed with one to three sequences.

The KCWI observations were conducted across the 2024B (4 nights; U267, PI: Hennawi), 2025A (3 nights; U275, PI: Hennawi), and 2025B (1 night; U262, PI: Hennawi) semesters. Approximately two nights in 2024B were not suitable for high-z quasar confirmation due to cloudy weather and/or poor seeing. In 2025A, 2.5 nights were lost to a shutter malfunction on Keck II, and the remaining half night was completed in June 2025. Observations in 2025B were successfully carried out in August 2025.

4.3. Keck/MOSFIRE

MOSFIRE is a NIR multi-object spectrograph on Keck I, covering the Y, J, H, and K bands. We primarily employed the Y band setting with a 1″ slit, providing a wavelength coverage of 972 –1125 nm and a spectral resolution of FWHM ≈ 126 km s^{-1} ($R \sim 2372$). Slits with widths of 0.″7, 1.″2, and 1.″5 were utilised depending on the seeing conditions. For candidates with photometric redshifts $z_{\rm phot} > 8.2$ (see Sect. 4.6), we switched to the $J2$ filter, whose wavelength coverage is 1117–1246 nm. Observations were carried out in an ABAB dither pattern with individual exposure times of 150 s. At least one dither sequence was obtained per target, corresponding to a minimum total integration time of 600 s.

MOSFIRE observations were carried out during the 2024B (4 nights; U418, PI: Hennawi), 2025A (5 nights; U275, N110, PI: Hennawi), and 2025B (0.5 nights; U262, PI: Hennawi) semesters. Approximately one half-night in 2024B and 1.5 nights in 2025A were compromised by poor seeing and/or substantial extinction. The 2025B observations were conducted under seeing conditions exceeding 2″.

4.4. Magellan/FIRE

FIRE is a NIR cross-dispersed echelle spectrograph on the Magellan Baade 6.5 m telescope. For confirmation of quasar candidates, we used FIRE in its long-slit (prism) mode with a 1.″0 slit, providing a spectral resolution of FWHM ∼ 1000–1660 km s^{-1} ($R \sim$ 180–300) and covering a wavelength range of 820–2500 nm. We obtained a typical on-source exposure time of 900 s × 2 per target, in an AB nodding sequence.

Observations were carried out during 2024B (4 nights; PI: J. Yang) and 2025A (0.5 nights; PI: X. Fan). In a few cases (e.g., due to faint targets or poor weather conditions), we increased the exposure time to 900 s × 4.

For one newly identified quasar, we also took 3.25 hours of Echelle mode observations for high-resolution and high-quality NIR spectra (see Fig. 7). The Echelle mode provides a spectral resolution of $R \sim 4800$ for a 0.″75 slit.

4.5. LBT/MODS and LBT/LUCI

MODS is an optical dual-channel spectrograph, and LUCI is a NIR imager and multi-object spectrograph on the LBT, covering the Y, J, H, and K bands. LBT Observations were carried out between February and September 2025 in 2025A (ID: MPIA-2025A-007) and 2025B (ID: MPIA-2025B-004) semesters. We used the binocular mode with the red grating for MODS and the G200 grating with $zJ + zJ$ filters for LUCI. The MODS red grating covers a wavelength range of 580–1000 nm, while LUCI G200 with zJ filters spans 900–1200 nm. We employed long-slit spectroscopy with slit widths of 1''.0–1''.2 and utilised an ABBA dithering pattern for optimal sky subtraction. Individual exposure times were 300 or 600 s for MODS and 240 s for LUCI, with total integration times of 1–2 hours for most targets.

We also performed a deep LUCI follow-up observation of EUCL J1729+6410 (see Fig. 6), the highest redshift quasar reported in this work. The total on-source exposure time is 2.8 hours in binocular mode with an average seeing of 0''.6.

4.6. Observation strategy and data reduction

To estimate the required exposure times for spectroscopic confirmation, we leveraged the photometric redshifts provided by the suite of algorithms described in Sect. 3, in combination with the fake source injection approach introduced by Yang et al. (2024). In brief, this method involves injecting synthetic quasar spectra with a given redshift and J-band magnitude into real 2D spectroscopic data. We then determined the minimum exposure time necessary for each instrument to yield a sufficient S/N for visually identifying the Lyman break. These exposure time estimates only serve as reference values and lower limits, due to the uncertainties in $z_{\rm phot}$ and the variability of observing conditions. They turned out to be robust for typical quasars overall.

For candidates in the north, we typically conducted initial observations with Keck/LRIS or Keck/KCWI, followed by Keck/MOSFIRE if there was no signal detected at the position of the target in the two optical instruments and $z_{\rm phot}$ suggested a potentially higher redshift. In contrast, for southern targets, the longslit mode of Magellan/FIRE, covering the full wavelength range from 800 nm to 2500 nm, enabled us to perform comprehensive spectroscopic follow-up without switching between instruments.

During observations, we conducted on-the-fly data reduction with `PypeIt` (Prochaska et al. 2020) for real-time decision-making. All spectra presented in this work were subsequently reduced in a uniform manner using `PypeIt`.

5. Discovery of 31 new high-z quasars

We have conducted spectroscopic follow-up of 123 high-z quasar candidates with the aforementioned observations. With these observations, we have identified 31 new quasars at redshifts $6.6 < z < 7.8$, whose discovery spectra are shown in Fig. 2 ($z \geq 6.9$) and Fig. 3 ($z < 6.9$). The cutouts of all the new quasars are displayed in Appendix B, and their 2D spectra are also shown in Appendix C. The summary of the rest of the candidates is provided in Sect. 5.2. Notably, 12 of these quasars lie at $z \geq 7$, more than doubling the number of known quasars at $z \geq 7$ prior to *Euclid*. Among them, EUCL J1729, at $z \approx 7.77$, is the most distant quasar known thus far.

Table A.3 summarises the key properties of the newly identified quasars, including their *Euclid* names[1], estimated redshifts, $J_{\rm E}$-band coordinates, photometry, rest-frame ultraviolet absolute magnitudes (M_{1450}), and bolometric luminosities ($L_{\rm bol}$). Redshifts were estimated based on the location of the Lyα emission line and/or the onset of the Gunn–Peterson trough (Gunn & Peterson 1965). The typical redshift uncertainty of such visual determinations is approximately 0.05–0.1 (e.g. Matsuoka et al. 2016); however, in extreme cases where Lyα is weak or strongly absorbed (see note b in Table A.1), the uncertainty can increase to ~0.2. The M_{1450} values were derived from the observed $J_{\rm E}$-band magnitudes by extrapolating a power-law continuum ($F_\lambda \propto \lambda^\alpha$) with a fixed spectral slope of $\alpha = -1.7$ (e.g. Telfer et al. 2002). Bolometric luminosities were converted from M_{1450} using the empirical conversion from Runnoe et al. (2012).

Figure 4 shows the distribution of the newly discovered quasars in the colour–colour diagrams ($I_{\rm E} - Y_{\rm E}$ versus $Y_{\rm E} - J_{\rm E}$ and $J_{\rm E} - H_{\rm E}$ versus $Y_{\rm E} - J_{\rm E}$). We overplotted the synthetic colour track of high-z quasars (D. Yang et al., in prep.) and the empirical brown-dwarf track from Euclid Collaboration: Barnett et al. (2019), both convolved with typical *Euclid* photometric noise. The new quasars lie close to the mean quasar track while exhibiting noticeable scatter, consistent with the diversity seen in the synthetic high-z quasar samples.

Figure 5 presents the distribution of redshift versus M_{1450} for the high-z quasars discovered in this work (red squares). For comparison, we also show previously known quasars (grey and green circles; Fan et al. 2023) LBGs (yellow circles; Matsuoka et al. 2016, 2018a,b, 2019a, 2022, 2025; Bouwens et al. 2022; Roberts-Borsani et al. 2024, 2025; Harikane et al. 2025) and active galactic nuclei (AGN; $L_{\rm bol} \lesssim 10^{45.5}$ erg s^{-1}) candidates from various JWST programs that have rest-frame ultraviolet (UV) spectroscopic observations (green triangles; Harikane et al. 2023; Kokorev et al. 2023; Larson et al. 2023; Maiolino et al. 2024; Schindler et al. 2025; Lin et al. 2026). The discoveries of these less luminous quasars in this work probe a previously unexplored region of parameter space, reaching lower luminosities ($M_{1450} \sim -24$) at $z \gtrsim 7$. The implications of these faint high-redshift quasars are discussed in Sect. 6.

5.1. Notes on individual quasars

EUCL J172902.75+641018.1: EUCL J1729 is the most distant quasar discovered to date, with $z \approx 7.77$. Figure 6 displays its 2D and 1D LBT/LUCI spectrum with a total integration time of 10 080 s (2.80 h). Based on visual inspection of the multiple emission features (Lyα, N V, O I, Si IV) shown up in the spectrum, we adopt a conservative redshift uncertainty of $\Delta z \lesssim 0.05$ for this target. The age of the Universe at its redshift is approximately 662 Myr. The redshift increment over the previous record-holder (Wang et al. 2021) is approximately 0.13, corresponding to ~15 Myr. Notably, a broad absorption feature is present blueward of the N V emission line, suggesting that EUCL J1729 is likely a broad absorption line (BAL)

[1] The naming convention for sources identified in this work follows the standard IAU format, with the prefix 'EUCL' denoting selection from *Euclid* data, followed by the J2000.0 right ascension and declination coordinates in $J_{\rm E}$ band. The final digits in both the RA and Dec components of the source names reflect a positional precision that is consistent with *Euclid*'s astrometric accuracy, which is better than 100 mas.

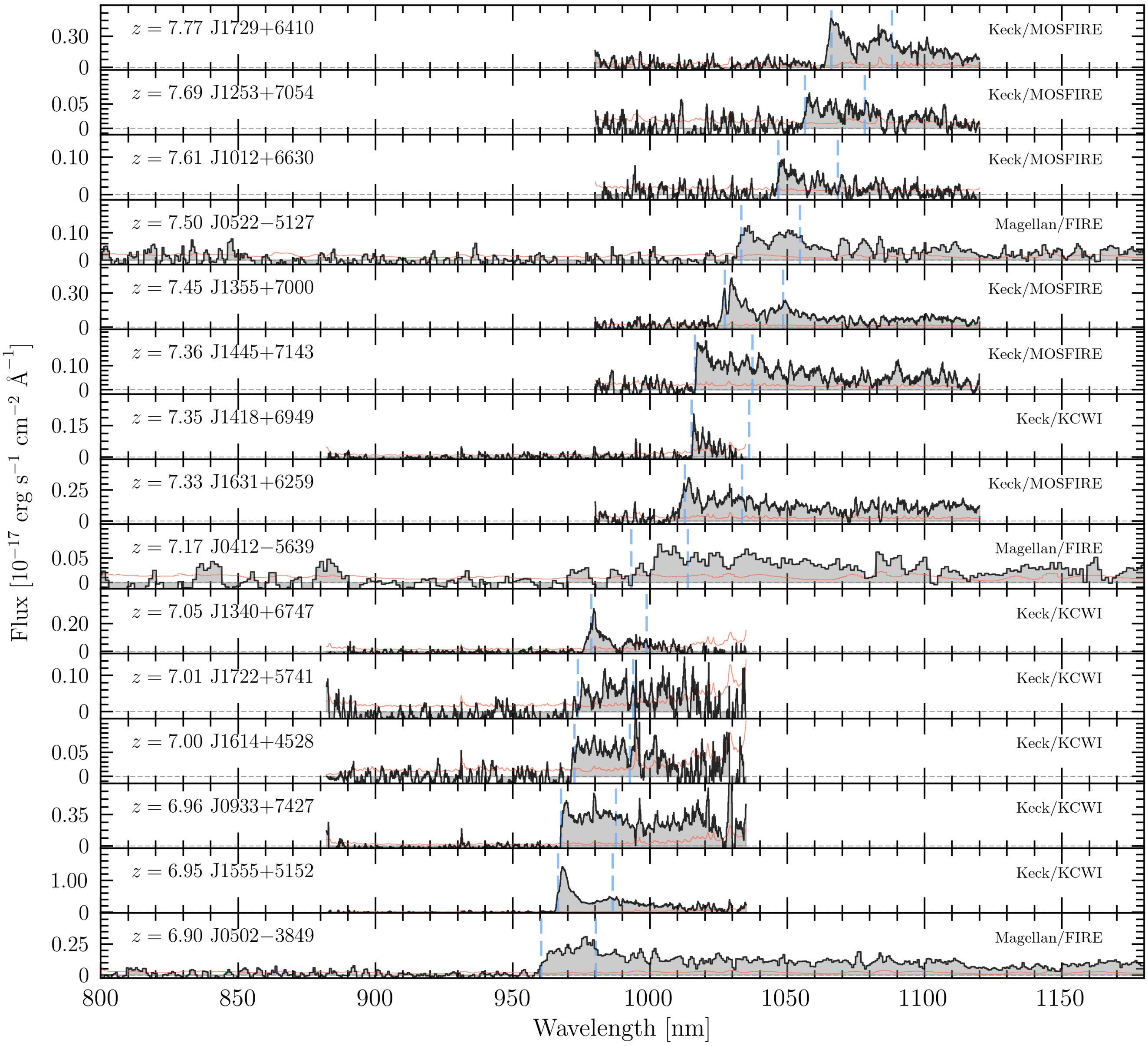

Fig. 2. Discovery spectra of the new quasars at $z \geq 6.9$. The redshifts estimated from the Lyα breaks, the short names, and the instruments for the discoveries are noted in the each panels. The spectra are fluxed, but not corrected for telluric absorption. They are also smoothed with inverse-variance weights and a 3 or 11 pixel window for Magellan or Keck, respectively. The red curves in each panel show the smoothed noise vectors. The dashed, vertical light blue lines indicate the positions of Lyα and N V lines.

or mini-BAL quasar. The O I and Si IV emission lines are also detected, with tentative, relatively narrow absorption features seen in their vicinity.

EUCL J125308.55+705432.3, EUCL J101255.87+663058.0: EUCL J1253 ($z \approx 7.69$) and EUCL J1012 ($z \approx 7.61$) are the second and third most distant quasars identified in this work. They are also the faintest known quasars at $z \gtrsim 7.5$, with $M_{1450} \sim -24$, making them nearly an order of magnitude less luminous in the rest-frame UV than the three previously known quasars at similar redshifts (see Fig. 5). They provide a unique opportunity to probe the faint end of the QLF at the highest redshifts currently accessible. Sub-millimetre follow-up observations of EUCL J1253 have revealed a large gas reservoir in its host galaxy. The data and the analysis will be presented in a companion paper (Belladitta et al., in prep.).

EUCL J052209.82−512709.2: We conducted an Echelle-mode observation of EUCL J0522 ($z \approx 7.50$) using Magellan/FIRE (see Sect. 4.4), as it is among the brightest $z > 7$ quasars identified in this work. However, its $J_{\rm E}$-band magnitude measured from the NIR stacked image is affected by hot pixels overlapping with the target, which bias the Euclid J_E photometry to be artificially brighter. We also note that the quasar probabilities computed by all methods were correspondingly impacted, and in particular were reduced relative to what would be obtained using the corrected photometry. At the time of writing, we have obtained a JWST/NIRSpec spectrum of this object. Using this spectrum and the $J_{\rm E}$-band transmission curve, we measured a corrected $J_{\rm E}$-band magnitude of 22.17. The full analysis of the JWST/NIRSpec data will be presented in a forthcoming publication.

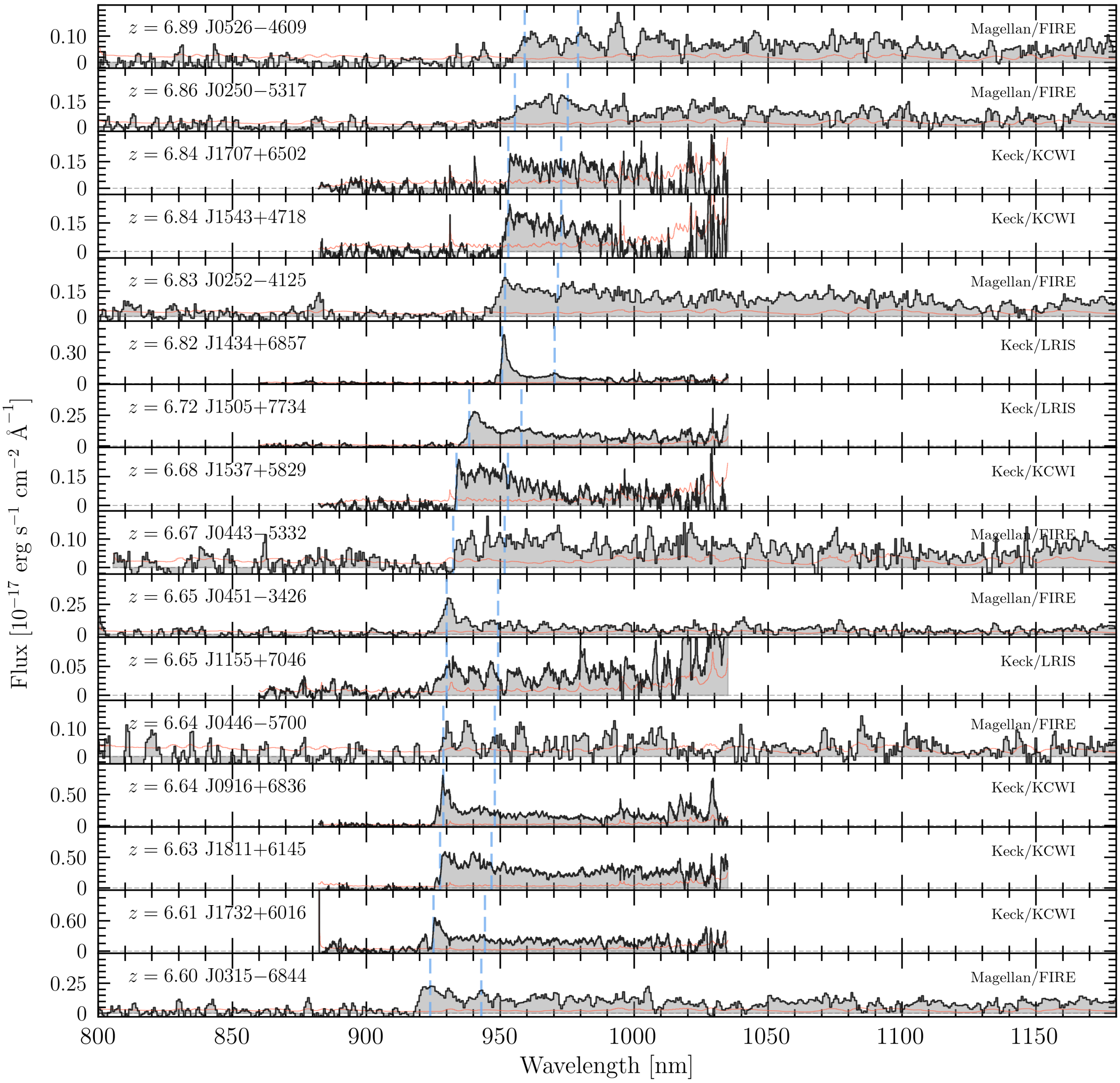

Fig. 3. Same as Fig. 2 but for the new quasars at $z < 6.9$.

Figure 7 shows the Echelle spectrum of this quasar with a total integration time of 11 700 s (3.25 h). Although EUCL J0522 is among the most luminous quasars at $z > 7$ in our sample, it remains approximately two magnitudes fainter than previously known quasars at comparable redshifts (see Fig. 5) in the rest-frame UV. The spectrum covers a broad rest-frame wavelength range, from Lyα to Mg II, and reveals several prominent emission features, including Lyα, N V, Si IV, C IV, and C III]. The Mg II line is not detected, likely due to insufficient S/N.

We fit the C IV emission line using a single-component Gaussian profile with the spectral fitting tool `Sculptor` (Schindler 2022), following the methodology described in Schindler et al. (2020). The fit yields a FWHM of C IV of approximately 2743 ± 400 km s^{-1}. Using the single-epoch black hole mass estimator based on the C IV line from Vestergaard & Peterson (2006), we derived $\log_{10}(M_{\rm BH}/M_{\odot}) \approx 7.6 \pm 0.4$ (the uncertainty is dominated by the scatter of the scaling relation, ~0.36 dex). This corresponds to an Eddington ratio of $\lambda_{\rm Edd} \approx 4.5$ for EUCL J0522. Assuming instead an Eddington-limited accretion rate ($\lambda_{\rm Edd} = 1$), the implied black hole mass would be $\log_{10}(M_{\rm BH}/M_{\odot}) \sim 8.25$. Given the limitations of C IV as a virial mass tracer (e.g., Coatman et al. 2016) and the modest S/N of the current data, a detailed analysis of the central black hole properties is deferred to future work using higher-quality data with wider spectral coverage, such as deeper JWST/NIRSpec observations.

EUCL J041250.73−563949.7, EUCL J134031.50+674715.1, EUCL J025029.93−531706.7, EUCL J044326.27−533214.9, EUCL J115522.89+704612.3: These objects represent the most apparent examples exhibiting atypical Lyα emission profiles. Such variations might suggest the presence of strong damping wing absorption, proximity damped Lyα systems

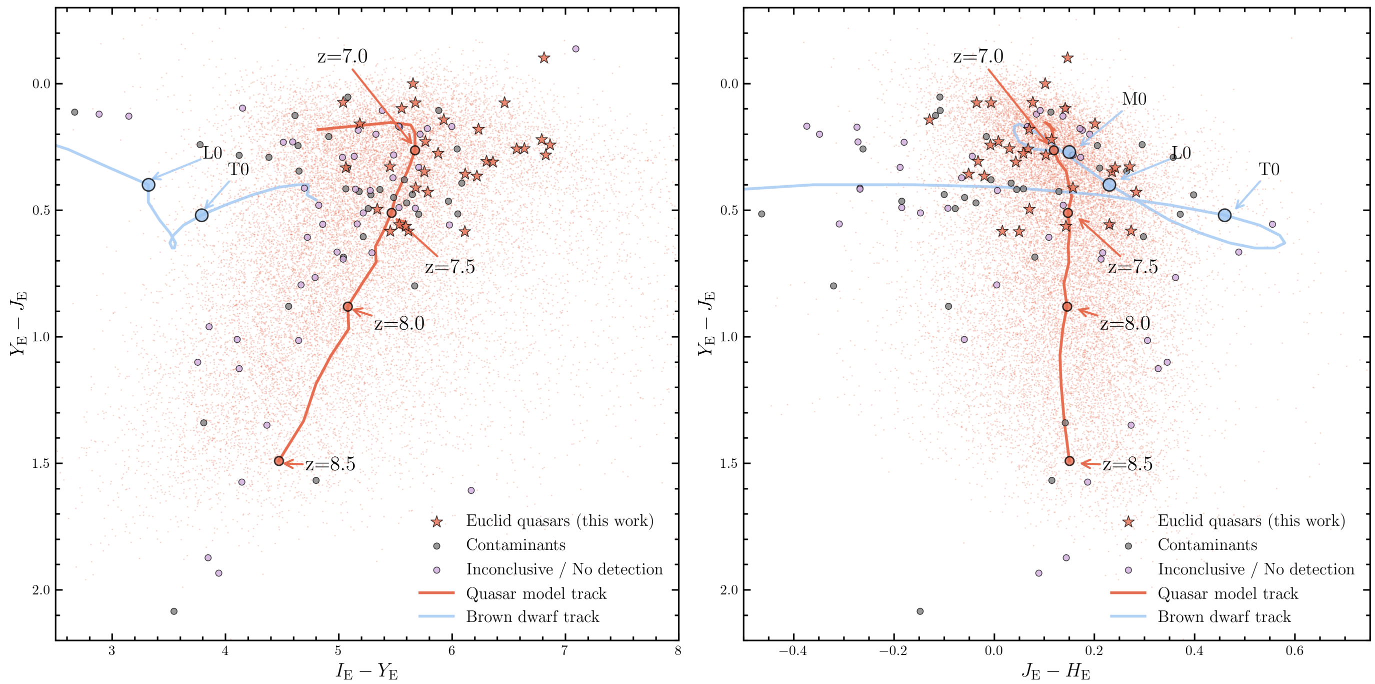

Fig. 4. Colour-colour diagrams of newly discovered quasars and other candidates. *Left*: $I_E - Y_E$ versus $Y_E - J_E$ colour-colour diagram. *Right*: $J_E - H_E$ versus $Y_E - J_E$ colour-colour diagram. The red stars mark the new *Euclid* quasars presented in this work, the grey circles denote the identified contaminants, and the violet circles are those marked as inconclusive or no detection (see Sect. 5.2). The red curve indicates the mean colour track of high-z quasars based on the synthetic quasar samples (the red points; Yang et al., in prep.), with redshifts of 7.0, 7.5, 8.0, and 8.5 annotated. The light blue curve represents the empirical brown-dwarf colour track from Euclid Collaboration: Barnett et al. (2019), with selected spectral types (M0, L0, T0) labelled.

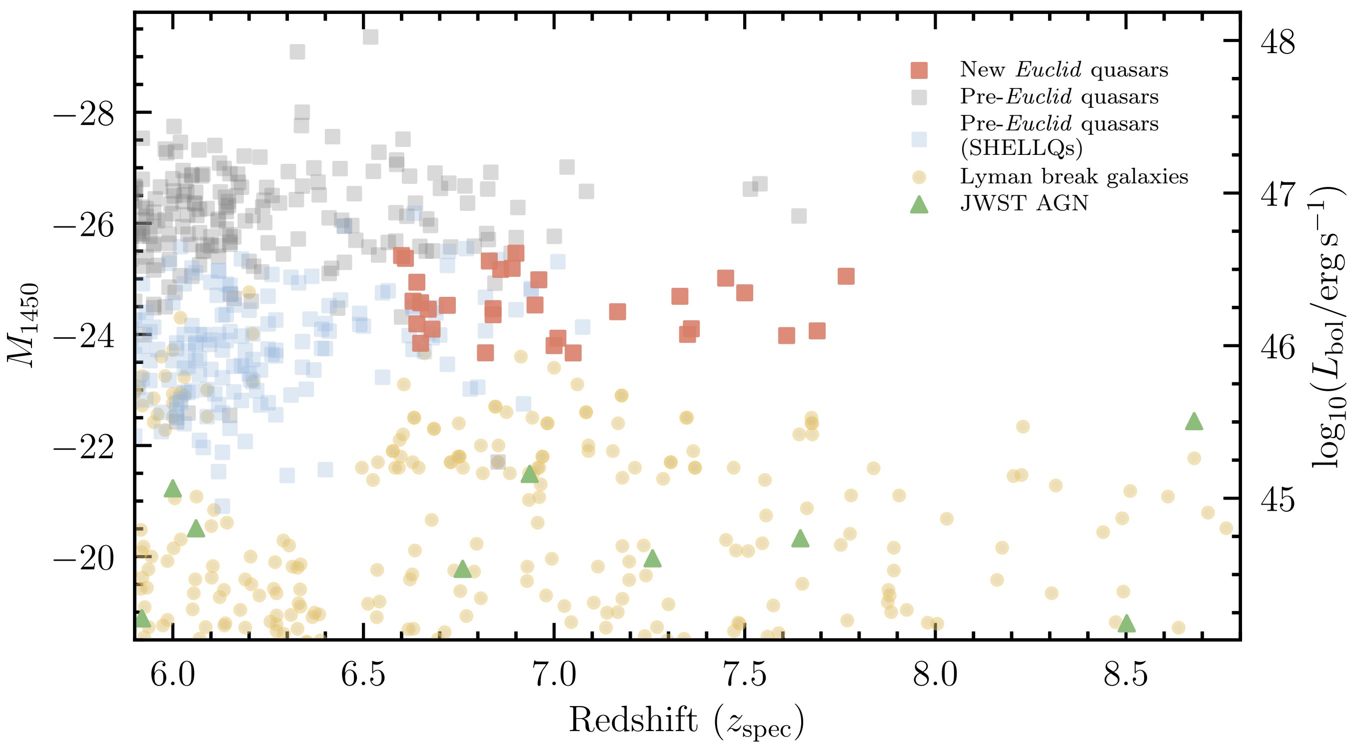

Fig. 5. Redshift versus absolute magnitude at 1450 Å, M_{1450}, for the new *Euclid*-discovered quasars (red squares), compared to pre-*Euclid* quasars (grey squares), including the SHELLQs sample (light blue squares). Yellow circles represent LBGs compiled from Matsuoka et al. (2016, 2018a,b, 2019a, 2022, 2025); Bouwens et al. (2022); Roberts-Borsani et al. (2024, 2025); Harikane et al. (2025). Green triangles denote faint AGN candidates discovered with JWST with rest-frame UV spectroscopic observation (Harikane et al. 2023; Kokorev et al. 2023; Larson et al. 2023; Maiolino et al. 2024; Schindler et al. 2025; Lin et al. 2026). The right-hand axis shows the corresponding bolometric luminosity scale converted from M_{1450}.

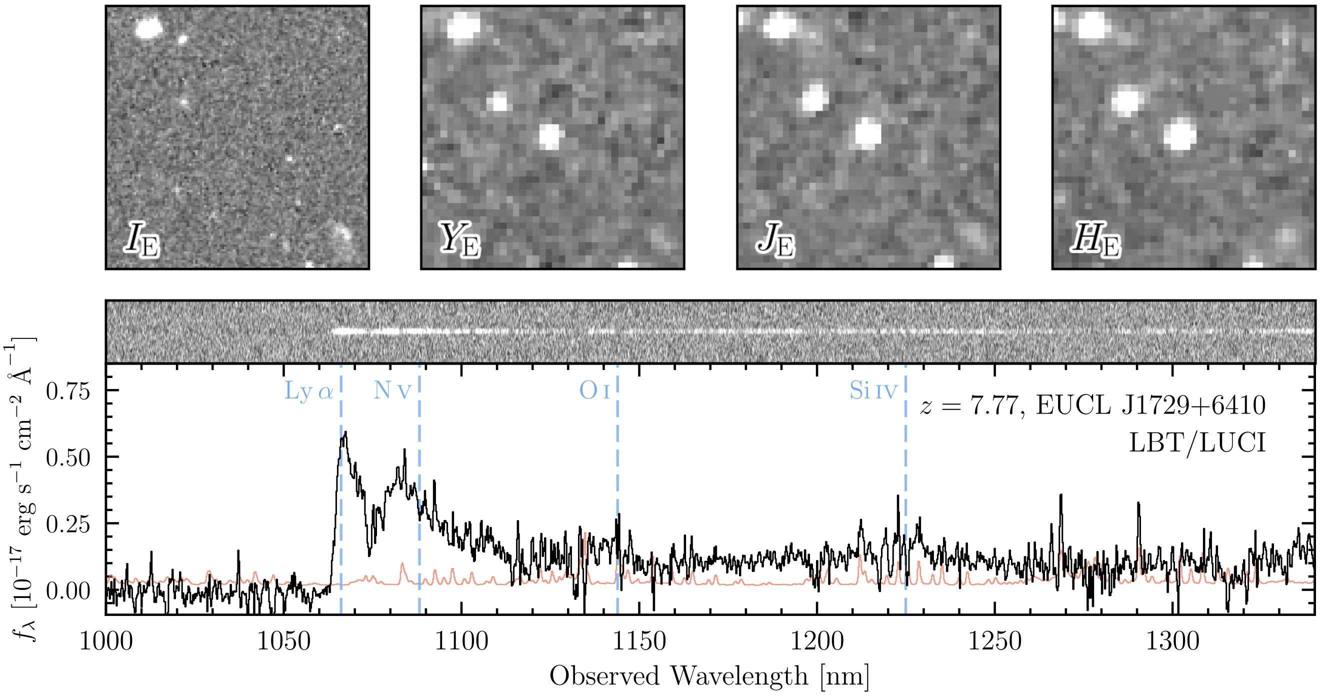

Fig. 6. *Euclid* cutouts and LBT/LUCI spectrum of EUCL J1729 ($z \approx 7.77$), the most distant quasar discovered to date. *Top*: 12″ × 12″ cutouts. From left to right: *Euclid* I_E, Y_E, J_E, and H_E bands. *Bottom*: The 1D spectrum has been smoothed using a 5 pixel inverse-variance-weighted boxcar. The total exposure time is 10 080 s.

(pDLAs), or, in some cases, the possibility that the sources are in fact luminous galaxies. However, we caution against over-interpreting these features based solely on the current discovery spectra – particularly those obtained with the Magellan prism mode – due to their low spectral resolution and modest S/N. Nevertheless, the diversity among UV-selected sources at the faint end ($M_{UV} \sim -24$; see Sect. 6) remains poorly constrained, and deeper spectroscopic follow-ups are essential to investigating their nature.

EUCL J091639.93+683652.9, EUCL J093330.60+742730.0: To identify new quasars with significant radio emission (>5σ), we cross-matched the LoTSS DR3 catalogues with our sample using a matching radius of 2″. Two quasars, EUCL J0916 ($z \approx 6.64$) and EUCL J0933 ($z \approx 6.96$), have positive matching results, as shown in Table 1. Their 144 MHz images, along with their *Euclid* cutouts, are presented in Fig. 8. It is worth noting that the association between the NIR and radio components of EUCL J0933 remains somewhat uncertain, as can be seen from the cutouts. However, given the low S/N (3.5) of the radio detection and the beam size of LoTSS (6″), the expected astrometric uncertainty is ~FWHM/(2 × S/N) ≈ 0″.9, so the 1″.76 offset corresponds to ~2σ and is not implausible for a real association. The corresponding 2D tail probability is of order 10%, much higher than the probability of random association between a LoTSS detection with S/N ≥ 3.5 and a $z \geq 6.5$ quasar. Assuming these fluxes are indeed from the quasars and a power-law index of 0.7, the radio powers at rest-frame 144 MHz are $\log_{10}\left(P_{144}/\mathrm{W\,Hz^{-1}}\right) \approx$ 26.64 and 26.19, respectively. These values place them among the most radio-luminous quasars known at $z > 6.5$ (e.g., Gloudemans et al. 2022), and are thus more naturally explained by quasar jet activity than by star formation in the host galaxy.

5.2. Notes on other candidates

We conducted spectroscopic observations for a total of 123 high-z quasar candidates. Of these, 31 were confirmed as quasars, while the remaining 92 were classified into three categories: 'contaminants', 'inconclusive' and 'no detection'. Table 2 summarises the classification scheme and definitions applied to these non-quasar sources. In Appendix D, we also show the 2D/1D spectra of some targets that were identified as 'contaminants', and the coordinates of all of them are provided in Table D.1.

A substantial fraction of the 'no detection' sources are likely to be contaminants based on their colours and z_{phot} estimates. This is supported by the fact that brown dwarfs and low-redshift red galaxies are generally more difficult to detect or classify than high-z quasars at similar J_E-band magnitudes. High-z quasars typically show a pronounced flux density near Lyα and a sharp break blueward of the line, while contaminants tend to exhibit a more gradual decline towards the blue end. Consequently, only sources with $z_{phot} \gtrsim 7$ that are undetected in the optical are retained as viable IR follow-up targets. Objects undetected in both the optical and NIR, or those with $z_{phot} < 7$ and no optical detection, are likely to be contaminants.

5.3. Composite spectra of Euclid high-z quasars

The rest-frame UV/optical SEDs of quasars are generally thought to exhibit little (if any), evolution with redshift (e.g., Shen et al. 2019; Yang et al. 2021; Onorato et al. 2025). To investigate this further, we constructed composite spectra for the $z > 7$, $z < 7$, and full quasar samples in this work. Each spectrum was shifted to the rest frame using its systemic redshift and re-binned onto a common rest-frame wavelength grid with a velocity spacing of Δv = 300 km s^{-1} per pixel. To normalise the spectra, we calculated the average flux density between 1250 and 1400 Å and scaled each spectrum to match the composite

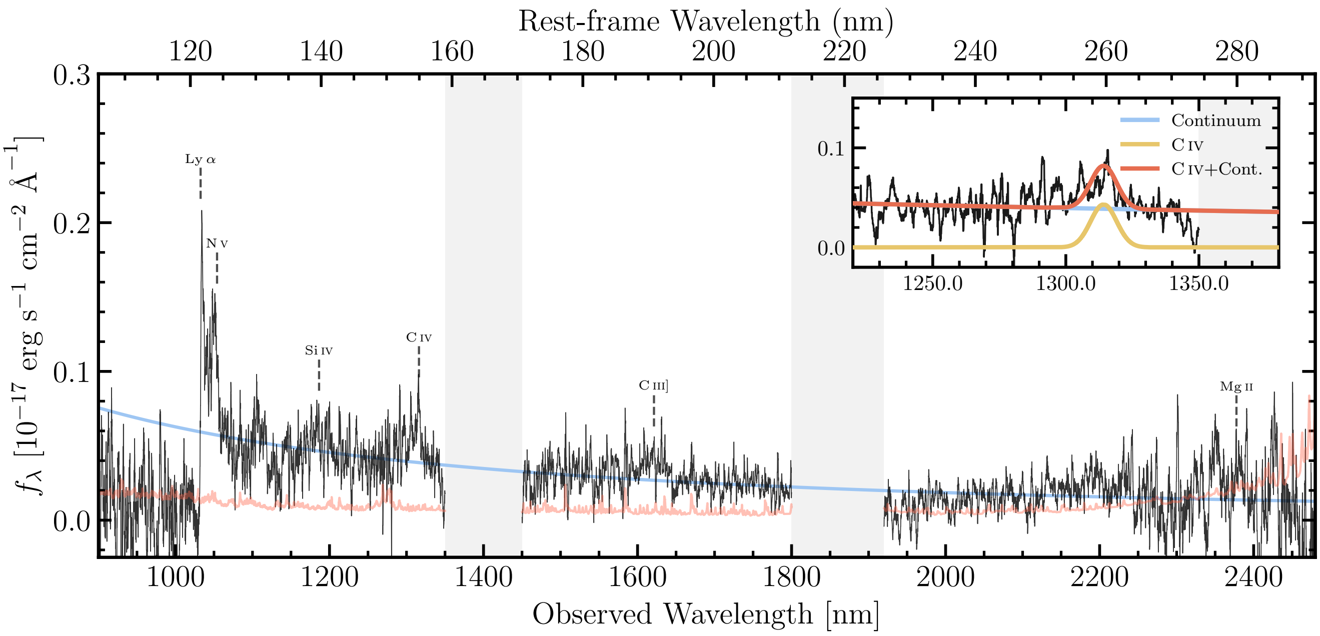

Fig. 7. Magellan/FIRE echelle spectrum of EUCL J0522, one of the brightest $z \sim 7.5$ quasars in this work ($J_E \approx 22.17$). The total integration time is 11 700 s. The black line shows the observed spectrum, inverse-variance smoothed with a 31 pixel boxcar. The light red curve shows the smoothed noise vector. The blue curve represents the best-fit power-law continuum. Locations of typical emission lines seen in a quasar spectrum are marked by vertical dashed lines, including Lyα, N V, Si IV, C IV, C III], and Mg II. Grey shaded regions indicate wavelength ranges heavily affected by telluric absorption. The inset displays the C IV region with the best-fit emission-line model generated using `Sculptor`, showing the individual C IV component (yellow), continuum (blue), and combined fit (red).

Table 1. Radio properties of the two *Euclid* quasars with LOFAR counterparts.

Target	Redshift	$S_{144\,\mathrm{MHz}}$ (mJy)	Separation
EUCL J0916	6.60	1.53 ± 0.25	0.″69
EUCL J0933	6.96	0.49 ± 0.14	1.″76

Notes. Both quasars are detected in the LoTSS DR3 catalogue with $>5\sigma$ significance in peak flux. The quoted values are integrated 144 MHz flux densities and their associated uncertainties. The angular separation indicates the distance between the J_E-band and radio positions. The beam size of LoTSS DR3 is around 6″.

spectrum from Onorato et al. (2025) over the same interval. Median-stacked spectra were then generated for the $z > 7$, $z < 7$, and full samples. The resulting composite spectra are shown in Fig. 9, alongside the Onorato et al. (2025) composite spectrum for comparison.

The $z > 7$ composite spectrum appears to exhibit stronger Lyα emission relative to the $z < 7$ counterpart, which may seem to contradict expectations of stronger damping wing absorption at higher redshifts. This can be partially attributed to a higher fraction of 'weak Lyα' objects within the $z < 7$ sample. Whether the observed weakness of Lyα in these sources is intrinsic or primarily driven by the limited spectral resolution remains to be explored with future follow-up data. Furthermore, the composite spectrum constructed from all quasars in this work is broadly consistent with the stacked spectrum from Onorato et al. (2025), with the exception of a somewhat weaker Lyα region, which is potentially indicative of stronger damping wing absorption due to smaller proximity zone for quasars that are less luminous in the rest-UV (e.g., Ishimoto et al. 2020), and/or because the average redshift of our sample is higher than that of Onorato et al. (2026), which would imply a higher average IGM neutral fraction.

Finally, the good agreement outside the Lyα region reinforces the well-known lack of strong spectral evolution in quasar rest-frame UV spectra at high redshift, indicating a rapid establishment of the physical conditions in the broad-line region at early times.

6. Populating the faint end at z ≳ 7

As shown in Fig. 5, compared with the quasar samples prior to *Euclid*, most of the quasars reported in this work are notably faint in the rest-frame UV. In particular, those at $z \gtrsim 7$ are generally 1–2 mag fainter than the quasars discovered prior to *Euclid* at comparable redshifts. At $z < 7$, the new quasars exhibit luminosities similar to those found in the SHELLQs sample (Matsuoka et al. 2016, 2018a,b, 2019a, 2022). Here we briefly discuss the significance of the high-z sources in this luminosity range.

6.1. Quasars or galaxies?

The luminosity functions of quasars and LBGs appear to intersect at $M_{1450} \sim -23$ to -24 (e.g., Finkelstein & Bagley 2022; Matsuoka et al. 2023; Harikane et al. 2025; Marques-Chaves et al. 2026). Therefore, it is not unexpected that some of the faintest objects identified as 'quasars' might instead be bright high-z galaxies (e.g., Sobral et al. 2015; Matsuoka et al. 2022), particularly if they lack prominent broad Lyα emission (see the examples listed in Sect. 5.1). While deep NIR spectroscopic observations are required to confirm their true nature, we provide a preliminary assessment by testing their consistency with being point sources. We performed Markov chain Monte Carlo (MCMC) fitting with a Sérsic profile using

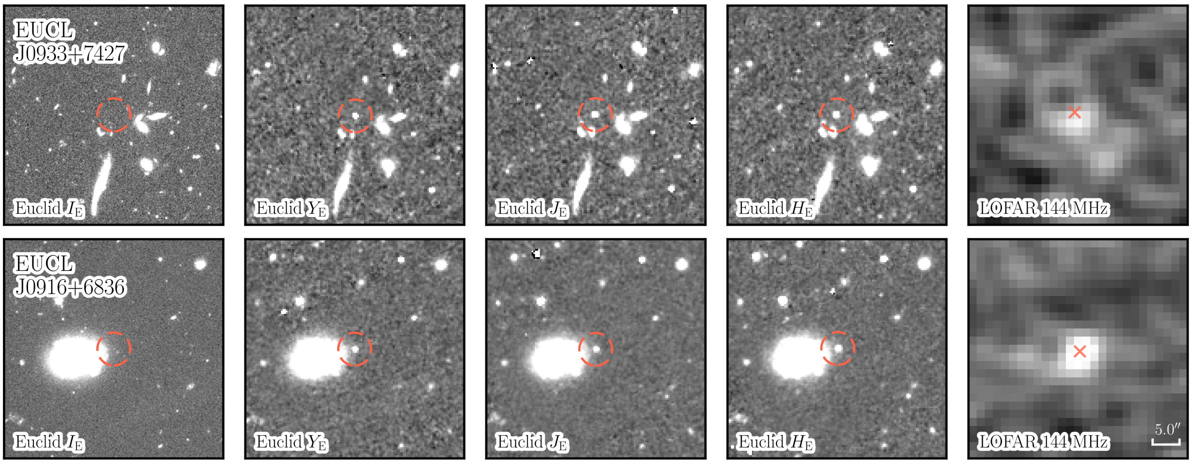

Fig. 8. Cutouts of two newly discovered LOFAR-detected quasars, EUCL J0933+7427 (bottom) at $z \approx 6.96$, and EUCL J0916+6836 (top) at $z \approx 6.6$. From left to right: *Euclid* I_E, Y_E, J_E, and H_E bands, followed by the LOFAR 144 MHz image. Each cutout covers $40'' \times 40''$ region. Red circles in *Euclid* images and red crosses in LOFAR images both denote the J_E-band positions of the quasars. A scale bar of a $5''$ length is shown in the last cutout.

Table 2. Classification of the remaining 92 candidates.

Label	Number	Description
Contaminants	45	A trace was detected but ruled out as a high-z quasar; 28 of the 45 were visually classified as possible brown dwarfs based on their spectral features.
Inconclusive	25	A trace was detected, but the data quality was insufficient to determine whether a Lyα break is present. Some remain high-priority targets for future observations.
No detection	22	No detectable flux was observed in the spectroscopic data.

pysersic (Pasha & Miller 2023) on the Y_E, J_E, and H_E images independently, and we subsequently multiplied the posterior distributions of the effective radius $R_{\rm eff}$ to get the combined posterior. The distribution of J_E magnitude versus the fitted $R_{\rm eff}$ is shown in Fig. 10.

The inferred $R_{\rm eff}$ of the sources from single-component Sérsic profile fitting are largely consistent with the J_E-band PSF: for all but one source, the posterior distribution of $R_{\rm eff}$ overlaps the J_E-band $R_{\rm EE50}$ (the radius enclosing 50% of the total energy; grey dashed line in Fig. 10) within the 1σ credible interval (Euclid Collaboration: Jahnke et al. 2025). The only exception is EUCL J1012+6630, for which the fit is likely affected by a nearby foreground source rather than the source being intrinsically extended. The Lyα line also appears relatively broad ($\gtrsim$1000 km s^{-1}), which is consistent with a quasar interpretation. As a comparison, we also show the size measurements for three newly identified faint brown dwarfs in our follow-up campaign. We further compare the inferred sizes with the empirical size-luminosity relations of $z \sim 7$ galaxies from Shibuya et al. (2015) and Sun et al. (2024). However, these relations do not place strong constraints on the very bright end as they're based on surveys in relatively small area. The intersection between the galaxy size-luminosity relations with the $R_{\rm EE50}$ line at $J_E \sim 24$ suggests that distinguishing quasars from galaxies based solely on their sizes in *Euclid* images becomes increasingly challenging for sources fainter than $J_E > 23$. Nevertheless, a further refinement of size measurements has the potential to exploit the diffraction-limited resolution of *Euclid*, enabling even tighter constraints to be placed on the sizes of faint objects.

6.2. Less luminous quasars as distinctive probes of the early Universe

High-z quasars at the luminous end, with $M_{1450} \lesssim -25$, are often referred to as the 'tip of the iceberg' and were thought to be unrepresentative of the broader SMBH population (see, e.g., Lauer et al. 2007; Li et al. 2022). Some observational studies indeed support this concern: less luminous quasars at $z \gtrsim 6$, such as those identified by SHELLQs and the CFHQS, appear to follow SMBH-galaxy mass relations more consistent with the local Universe (e.g., Willott et al. 2017; Izumi et al. 2019; Silverman et al. 2025), in contrast to their more luminous counterparts. At $z > 7$, however, such studies have been extremely limited: only one type-I quasar with $M_{1450} > -25$ was known prior to *Euclid* (Matsuoka et al. 2019b). The discoveries reported here significantly expand this regime, enabling systematic investigation of the demographics, accretion properties, and luminosity function of low-luminosity quasars at $z > 7$.

On the other hand, quasars with faint UV luminosities may exhibit more diverse behaviour, as shown in Sect. 5.1. Studies at $z \sim 6$ have already revealed intriguing properties in the host galaxies of similarly faint quasars: Onoue et al. (2025) detected Balmer absorption lines of stellar origin, a spectral signature commonly associated with post-starburst activity in the galaxies; Bouwens et al. (2025) reported that some low-luminosity quasars might reside in massive galaxies with stellar masses comparable to those hosting luminous quasars. Moreover, as mentioned earlier, at these luminosities the quasar and galaxy luminosity functions intersect, implying that it is also possible that some sources identified as quasars may in fact be exceptionally luminous star-forming galaxies (e.g., Marques-Chaves et al. 2022, at lower redshift). While such cases complicate classification, they are themselves of considerable interest, offering

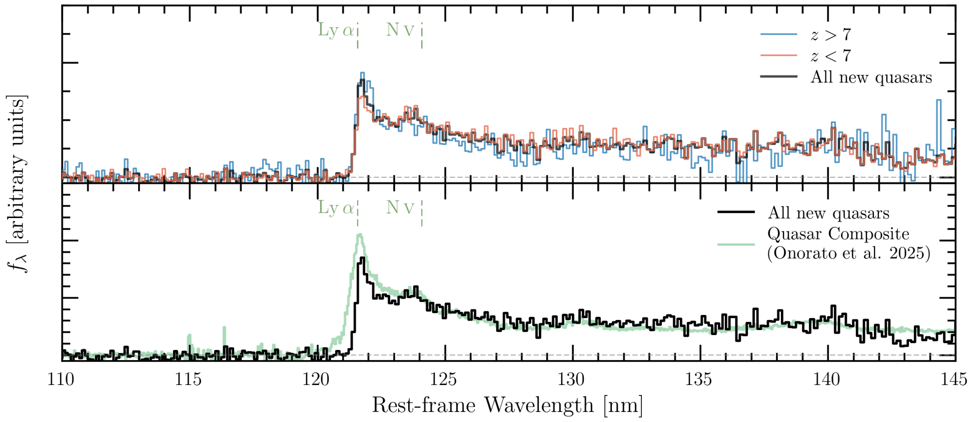

Fig. 9. Stacked rest-frame UV spectra of the new *Euclid* quasars. The top panel shows the stacked rest-frame UV spectra of all new *Euclid* quasars, the $z > 7$ sample, and the $z < 7$ sample. The bottom panel compares the stacked spectrum of all new quasars with a stacked spectrum of $z > 6.5$ bright quasars from Onorato et al. (2025). Each spectrum was shifted to the rest frame, rebinned onto a common grid with $\Delta v = 300\,\mathrm{km\,s^{-1}}$, and scaled to match a fiducial absolute magnitude of $M_{1450} = -24$. We show the median-stacked results here. No significant evolution is identified with these stacked spectra.

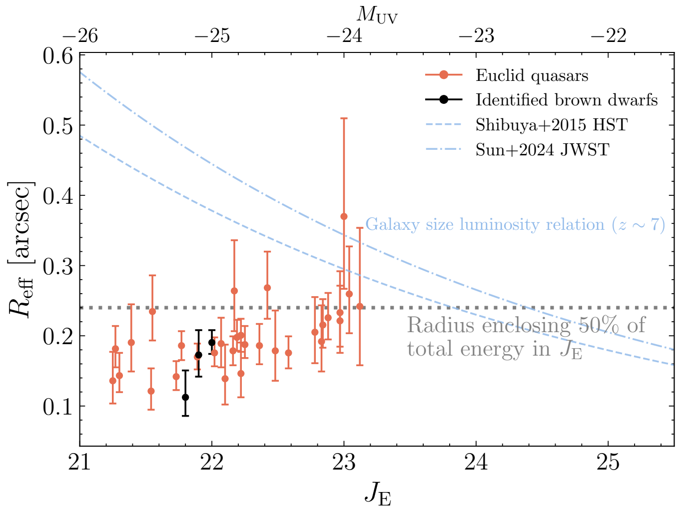

Fig. 10. Magnitude versus fitted size of *Euclid* quasars (red orange) and identified brown dwarfs (black) in the $J_{\rm E}$ band. The effective radii ($R_{\rm eff}$) are measured from *Euclid* $Y_{\rm E}$, $J_{\rm E}$, and $H_{\rm E}$ images assuming a Sersic profile. The light blue lines represent the empirical size-luminosity relations for galaxies at $z \sim 7$ (Shibuya et al. 2015; Sun et al. 2024). The grey horizontal line represents the 50% enclosed energy radius ($R_{\rm EE50}$; Euclid Collaboration: Jahnke et al. 2025) for the PSF of the $J_{\rm E}$ band. The *Euclid* quasars are consistent with being point sources.

insights into the most massive and actively star-forming systems in the early Universe (e.g., Marques-Chaves et al. 2026).

In addition, quasars with lower UV luminosities may also be important for reionisation studies. Their smaller proximity zones (e.g., Ishimoto et al. 2020; Onorato et al. 2026) imply more neutral surroundings, making them especially sensitive probes of the ionisation state of the IGM.

6.3. Future exploration toward even fainter regimes

We also note that the sensitivity limit of *Euclid* has not yet been reached. Most of the quasars reported here are brighter than $J_{\rm E} \sim 23$, whereas the 5σ depth of NISP imaging reaches AB ≈ 24.5. Identifying quasars at these fainter limits, however, is not feasible with ground-based spectroscopy: detecting a $z \gtrsim 7$ quasar with $J_{\rm E} \sim 23$ typically requires $\gtrsim$1–2 hours of integration on a 10-m telescope. For even fainter targets, utilising HST or JWST will be the only viable option.

Nevertheless, such faint samples are of irreplaceable value. JWST has recently revealed a population of EoR sources with broad Balmer emission lines, possibly indicative of active SMBHs (e.g., Harikane et al. 2023; Larson et al. 2023; Kokorev et al. 2023; Lin et al. 2024; Greene et al. 2024; Maiolino et al. 2024; Matthee et al. 2024). However, these sources differ from classical type-I quasars in important respects: they often lack strong high-ionisation lines, and show varied behaviour in variability (e.g., Kokubo & Harikane 2025; Tee et al. 2025), X-ray emission (Ananna et al. 2024; Yue et al. 2024), radio detection (e.g., Perger et al. 2025; Gloudemans et al. 2025), and mid-IR torus emission (e.g., Akins et al. 2025). Their number densities also exceed predictions from QLF extrapolations by factors of 10–100 (e.g., Harikane et al. 2023; Pizzati et al. 2025). Building quasar samples down to $M_{\rm UV} \gtrsim -22$ – comparable to the brightest JWST-identified AGN – will be essential to elucidate the connections and distinctions between quasar, galaxy, and JWST AGN populations.

7. Summary

Euclid has long been anticipated to revolutionise the search for high-z quasars. In this work, we demonstrate that this potential is now being realised: within the first one and a half year of the EWS ($\sim$3000 deg^2), we have uncovered 31 new quasars spanning the redshift range $6.6 < z < 7.8$ (see Fig. 2 and Table A.1). Notably, 12 of these quasars lie at $z \geq 7$, more than doubling the number of known quasars at these redshifts prior to *Euclid*. Among them, EUCL J1729+6410, at $z \approx 7.77$ with $M_{1450} \approx -25.05$, currently represents the most distant quasar known (see Fig. 6). A large fraction of the newly discovered quasars are also on the faint end of the QLF, with $M_{1450} \sim -24$ (see Fig. 5). Furthermore, two of the newly discovered quasars show significant ($>5\sigma$) radio counterparts in the LoTSS, underscoring the promising synergy between *Euclid* and LOFAR in identifying and characterising the high-z quasar population at $z \sim 7$ and beyond. These discoveries mark a substantial advance into the epoch of cosmic reionisation, showcasing *Euclid*'s unprecedented capability to extend the redshift frontier of quasar studies. Follow-up observations are already underway, although many of these sources are faint and challenging to characterise spectroscopically (see Fig. 5). Facilities such as JWST, NOEMA, and ALMA, will be crucial for future characterization.

Finally, the results presented here are broadly consistent with the forecast of Euclid Collaboration: Barnett et al. (2019), according to which $\sim$20 quasars should exist at $z \gtrsim 7$ in

3000 deg^2 down to $J_{\rm E} \sim 23$, while this work has already yielded 14 such quasars among 31 new discoveries. Because our search and spectroscopic follow-up are not yet complete (particularly in the south, where fewer confirmation resources have been available), this comparison is provisional; nevertheless, it could be suggestive that some existing QLFs underpredict the number density at $z \gtrsim 7$ and/or at the faint end. We caution against over-interpreting this possible tension pending a formal analysis of the selection function and luminosity function. Finally, as the *Euclid* footprint expands and confirmations proceed smoothly, the first $z > 8$ quasars are likely to be identified in the near future.

Data availability

This work has made use of Euclid data from the European Space Agency (ESA) mission Euclid. The quasar cutouts are available at `https://doi.org/10.57780/esa-50769fd`. The discovery spectra are available from the corresponding author upon reasonable request.

Acknowledgements. D. Yang acknowledges helpful discussions with members of the ENIGMA group at UC Santa Barbara and Leiden University, in particular Elia Pizzati, Silvia Onorato, and Diego González for their valuable feedback. D. Yang thanks Shane Bechtel for assistance during observations, and acknowledges the early contributions of Riccardo Nanni, which helped lay the foundation for this work. D. Yang and J. F. Hennawi acknowledge support from the European Research Council (ERC) under the European Union's Horizon 2020 research and innovation program (grant agreement No 885301). J. F. Hennawi acknowledges support from NSF grant No. 2307180. F. Guarneri and J.-T. Schindler are supported by the Deutsche Forschungsgemeinschaft (DFG, German Research Foundation) – Project number 518006966. F. Wang acknowledges support from NSF award AST-2513040. R. Decarli acknowledges support from the INAF GO 2022 grant "The birth of the giants: JWST sheds light on the build-up of quasars at cosmic dawn", INAF Minigrant 2024 "The interstellar medium at high redshift", and by the PRIN MUR "2022935STW", RFF M4.C2.1.1, CUP J53D23001570006 and C53D23000950006. S. E. I. Bosman is supported by the Deutsche Forschungsgemeinschaft (DFG) under Emmy Noether grant number BO 5771/1-1. Y. Harikane acknowledges support from the Japan Society for the Promotion of Science (JSPS) Grant-in-Aid for Scientific Research (24H00245), the JSPS Core-to-Core Program (JPJSCCA20210003), and the JSPS International Leading Research (22K21349). J. R. Weaver acknowledges that support for this work was provided by The Brinson Foundation through a Brinson Prize Fellowship grant. The Euclid Consortium acknowledges the European Space Agency and a number of agencies and institutes that have supported the development of *Euclid*, in particular the Agenzia Spaziale Italiana, the Austrian Forschungsförderungsgesellschaft funded through BMIMI, the Belgian Science Policy, the Canadian Euclid Consortium, the Deutsches Zentrum für Luft- und Raumfahrt, the DTU Space and the Niels Bohr Institute in Denmark, the French Centre National d'Etudes Spatiales, the Fundação para a Ciência e a Tecnologia, the Hungarian Academy of Sciences, the Ministerio de Ciencia, Innovación y Universidades, the National Aeronautics and Space Administration, the National Astronomical Observatory of Japan, the Netherlandse Onderzoekschool Voor Astronomie, the Norwegian Space Agency, the Research Council of Finland, the Romanian Space Agency, the State Secretariat for Education, Research, and Innovation (SERI) at the Swiss Space Office (SSO), and the United Kingdom Space Agency. A complete and detailed list is available on the *Euclid* web site (`www.euclid-ec.org`). Some of the data presented herein were obtained at Keck Observatory, which is a private 501(c)3 non-profit organization operated as a scientific partnership among the California Institute of Technology, the University of California, and the National Aeronautics and Space Administration. The Observatory was made possible by the generous financial support of the W. M. Keck Foundation. The authors wish to recognise and acknowledge the very significant cultural role and reverence that the summit of Maunakea has always had within the Native Hawaiian community. We are most fortunate to have the opportunity to conduct observations from this mountain. This paper includes data gathered with the 6.5 meter Magellan Telescopes located at Las Campanas Observatory, Chile. This work uses LBT data from programmes: MPIA-2025A-007 and MPIA-2025B-004. The LBT is an international collaboration among institutions in the United States, Italy and Germany. LBT Corporation partners are: The University of Arizona on behalf of the Arizona university system; Istituto Nazionale di Astrofisica, Italy; LBT Beteiligungsgesellschaft, Germany, representing the Max-Planck Society, the Astrophysical Institute Potsdam, and Heidelberg University; The Ohio State University, and The Research Corporation, on behalf of The University of Notre Dame, University of Minnesota, and University of Virginia, LOFAR data products were provided by the LOFAR Surveys Key Science project (LSKSP; `https://lofar-surveys.org/`) and were derived from observations with the International LOFAR Telescope (ILT). LOFAR is the Low Frequency Array designed and constructed by ASTRON. It has observing, data processing, and data storage facilities in several countries, which are owned by various parties (each with their own funding sources), and which are collectively operated by the ILT foundation under a joint scientific policy. The efforts of the LSKSP have benefited from funding from the European Research Council, NOVA, NWO, CNRS-INSU, the SURF Co-operative, the UK Science and Technology Funding Council and the Jülich Supercomputing Centre. We make use of z-band imaging from the Wide Imaging with Subaru HSC of the Euclid Sky (WISHES) program operated by the Subaru Telescope, which is operated by the National Astronomical Observatory of Japan. We also make use of z-band imaging from the Dark Energy Survey (DES), based on observations obtained at the Cerro Tololo Inter-American Observatory, National Optical Astronomy Observatory, which is operated by AURA under a cooperative agreement with the National Science Foundation. This work made use of `NumPy` (Harris et al. 2020), `SciPy` (Virtanen et al. 2020), `Astropy` (Astropy Collaboration 2013, 2018, 2022), `PypeIt` (Prochaska et al. 2020), `Sculptor` (Schindler 2022), `condXD` (Kang et al. 2025), `pysersic` (Pasha & Miller 2023), `Matplotlib` (Hunter 2007), `corner.py` (Foreman-Mackey 2016), `healpy` (Zonca et al. 2020).

References

Akins, H. B., Casey, C. M., Lambrides, E., et al. 2025, ApJ, 991, 37
Ananna, T. T., Bogdán, Á., Kovács, O. E., Natarajan, P., & Hickox, R. C. 2024, ApJ, 969, L18
Arnouts, S., & Ilbert, O. 2011, Astrophysics Source Code Library [record ascl:1108.009]
Astropy Collaboration (Robitaille, T. P., et al.) 2013, A&A, 558, A33
Astropy Collaboration (Price-Whelan, A. M., et al.) 2018, AJ, 156, 123
Astropy Collaboration (Price-Whelan, A. M., et al.) 2022, ApJ, 935, 167
Bañados, E., Venemans, B. P., Mazzucchelli, C., et al. 2018, Nature, 553, 473
Bañados, E., Le Brun, V., Belladitta, S., et al. 2025a, MNRAS, 542, 1088
Bañados, E., Momjian, E., Connor, T., et al. 2025b, Nat. Astron., 9, 293
Bertin, E. 2010, Astrophysics Source Code Library [record ascl:1010.068]
Bertin, E. 2013, Astrophysics Source Code Library [record ascl:1301.001]
Bertin, E., & Arnouts, S. 1996, A&AS, 117, 393
Bosman, S. E. I., Davies, F. B., Becker, G. D., et al. 2022, MNRAS, 514, 55
Bosman, S. E. I., Álvarez-Márquez, J., Davies, F. B., et al. 2025, ApJ, submitted [arXiv:2511.02902]
Bouwens, R. J., Smit, R., Schouws, S., et al. 2022, ApJ, 931, 160
Bouwens, R. J., Banados, E., Decarli, R., et al. 2025, A&A, submitted [arXiv:2506.24128]
Bovy, J., Hogg, D. W., & Roweis, S. T. 2011, Ann. Appl. Stat., 5, 1657
Bradley, L., Sipocz, B., Robitaille, T., et al. 2016, Astrophysics Source Code Library [record ascl:1609.011]
Brammer, G. B., van Dokkum, P. G., & Coppi, P. 2008, ApJ, 686, 1503
Calderone, G., Guarneri, F., Porru, M., et al. 2024, A&A, 683, A34
Chen, T., & Guestrin, C. 2016 in Proceedings of the 22nd ACM SIGKDD International Conference on Knowledge Discovery and Data Mining, (New York, NY, USA: Association for Computing Machinery), KDD'16, 785
Coatman, L., Hewett, P. C., Banerji, M., & Richards, G. T. 2016, MNRAS, 461, 647
Dark Energy Survey Collaboration (Abbott, T., et al.) 2016, MNRAS, 460, 1270
Davies, F. B., Hennawi, J. F., Bañados, E., et al. 2018, ApJ, 864, 142
Davies, F. B., Bosman, S. E. I., D'Odorico, V., et al. 2026, MNRAS, 545, staf1862
Dawson, K. S., Schlegel, D. J., Ahn, C. P., et al. 2013, AJ, 145, 10
Dawson, K. S., Kneib, J.-P., Percival, W. J., et al. 2016, AJ, 151, 44
Dye, S., Lawrence, A., Read, M. A., et al. 2018, MNRAS, 473, 5113
Edge, A., Sutherland, W., Kuijken, K., et al. 2013, Messenger, 154, 32
Eilers, A.-C., Mackenzie, R., Pizzati, E., et al. 2024, ApJ, 974, 275
Euclid Collaboration (Barnett, R., et al.) 2019, A&A, 631, A85
Euclid Collaboration (Scaramella, R., et al.) 2022, A&A, 662, A112
Euclid Collaboration (Schirmer, M., et al.) 2022, A&A, 662, A92
Euclid Collaboration (Cropper, M., et al.) 2025, A&A, 697, A2
Euclid Collaboration (Jahnke, K., et al.) 2025, A&A, 697, A3
Euclid Collaboration (Mellier, Y., et al.) 2025, A&A, 697, A1
Euclid Collaboration (McCracken, H. J., et al.) 2026, A&A, 711, A2
Euclid Collaboration (Polenta, G., et al.) 2026, A&A, 711, A3
Euclid Collaboration (Romelli, E., et al.) 2026, A&A, 711, A4
Ezziati, M., Pello, R., Cuby, J. G., et al. 2025, A&A, 701, A282
Fan, X., White, R. L., Davis, M., et al. 2000, AJ, 120, 1167
Fan, X., Bañados, E., & Simcoe, R. A. 2023, ARA&A, 61, 373

Farina, E. P., Schindler, J.-T., Walter, F., et al. 2022, ApJ, 941, 106
Finkelstein, S. L., & Bagley, M. B. 2022, ApJ, 938, 25
Foreman-Mackey, D. 2016 J. Open Source Softw., 1, 24
Fu, Y., Wu, X.-B., Bouwens, R. J., et al. 2025, ApJS, 279, 54
Gloudemans, A. J., Duncan, K. J., Saxena, A., et al. 2022, A&A, 668, A27
Gloudemans, A. J., Duncan, K. J., Eilers, A.-C., et al. 2025, ApJ, 986, 130
Greene, J. E., Labbe, I., Goulding, A. D., et al. 2024, ApJ, 964, 39
Greig, B., Mesinger, A., Bañados, E., et al. 2024, MNRAS, 530, 3208
Guarneri, F., Schindler, J. T., Meyer, R. A., et al. 2026, A&A, 709, A241
Gunn, J. E., & Peterson, B. A. 1965, ApJ, 142, 1633
Gwyn, S., McConnachie, A. W., Cuillandre, J.-C., et al. 2025, AJ, 170, 324
Harikane, Y., Zhang, Y., Nakajima, K., et al. 2023, ApJ, 959, 39
Harikane, Y., Inoue, A. K., Ellis, R. S., et al. 2025, ApJ, 980, 138
Harris, C. R., Millman, K. J., van der Walt, S. J., et al. 2020, Nature, 585, 357
Hennawi, J. F., Kist, T., Davies, F. B., & Tamanas, J. 2025, MNRAS, 539, 2621
Hunter, J. D. 2007, Comput. Sci. Eng., 9, 90
Inayoshi, K., Visbal, E., & Haiman, Z. 2020, ARA&A, 58, 27
Ishimoto, R., Kashikawa, N., Onoue, M., et al. 2020, ApJ, 903, 60
Izumi, T., Onoue, M., Matsuoka, Y., et al. 2019, PASJ, 71, 111
Jin, X., Yang, J., Fan, X., et al. 2023, ApJ, 942, 59
Kang, Y., Hennawi, J. F., Schindler, J.-T., Tamanas, J., & Nanni, R. 2025, MNRAS, 541, 2815
Kist, T., Hennawi, J. F., & Davies, F. B. 2025, MNRAS, 538, 2704
Kokorev, V., Fujimoto, S., Labbe, I., et al. 2023, ApJ, 957, L7
Kokubo, M., & Harikane, Y. 2025, ApJ, 995, 24
Kormendy, J., & Ho, L. C. 2013, ARA&A, 51, 511
Larson, R. L., Finkelstein, S. L., Kocevski, D. D., et al. 2023, ApJ, 953, L29
Lauer, T. R., Tremaine, S., Richstone, D., & Faber, S. M. 2007, ApJ, 670, 249
Lawrence, A., Warren, S. J., Almaini, O., et al. 2007, MNRAS, 379, 1599
Li, J., Silverman, J. D., Izumi, T., et al. 2022, ApJ, 931, L11
Lin, X., Wang, F., Fan, X., et al. 2024, ApJ, 974, 147
Lin, X., Fan, X., Wang, F., et al. 2026, ApJ, 996, 93
Maiolino, R., Scholtz, J., Curtis-Lake, E., et al. 2024, A&A, 691, A145
Marques-Chaves, R., Schaerer, D., Álvarez-Márquez, J., et al. 2022, MNRAS, 517, 2972
Marques-Chaves, R., Schaerer, D., Dessauges-Zavadsky, M., et al. 2026, A&A, in press, https://doi.org/10.1051/0004-6361/202557740
Martínez-Ramírez, L. N., Wolf, J., Belladitta, S., et al. 2026, A&A, 708, A117
Matsuoka, Y., Onoue, M., Kashikawa, N., et al. 2016, ApJ, 828, 26
Matsuoka, Y., Iwasawa, K., Onoue, M., et al. 2018a, ApJS, 237, 5
Matsuoka, Y., Onoue, M., Kashikawa, N., et al. 2018b, PASJ, 70, S35
Matsuoka, Y., Iwasawa, K., Onoue, M., et al. 2019a, ApJ, 883, 183
Matsuoka, Y., Onoue, M., Kashikawa, N., et al. 2019b, ApJ, 872, L2
Matsuoka, Y., Iwasawa, K., Onoue, M., et al. 2022, ApJS, 259, 18
Matsuoka, Y., Onoue, M., Iwasawa, K., et al. 2023, ApJ, 949, L42
Matsuoka, Y., Iwasawa, K., Onoue, M., et al. 2025, ApJS, 280, 68
Matthee, J., Naidu, R. P., Brammer, G., et al. 2024, ApJ, 963, 129
McGurk, R. C., Matuszewski, M., Neill, J. D., et al. 2024, SPIE Conf. Ser., 13096, 1309647
McLean, I. S., Steidel, C. C., Epps, H. W., et al. 2012, SPIE Conf. Ser., 8446, 84460J
McMahon, R. G., Banerji, M., Gonzalez, E., et al. 2013, Messenger, 154, 35
Miyazaki, S., Komiyama, Y., Kawanomoto, S., et al. 2018, PASJ, 70, S1
Morrissey, P., Matuszewski, M., Martin, D. C., et al. 2018, ApJ, 864, 93
Mortlock, D. J., Warren, S. J., Venemans, B. P., et al. 2011, Nature, 474, 616
Mortlock, D. J., Patel, M., Warren, S. J., et al. 2012, MNRAS, 419, 390
Nanni, R., Hennawi, J. F., Wang, F., et al. 2022, MNRAS, 515, 3224
Neeleman, M., Novak, M., Venemans, B. P., et al. 2021, ApJ, 911, 141
Oke, J. B., & Gunn, J. E. 1983, ApJ, 266, 713
Oke, J. B., Cohen, J. G., Carr, M., et al. 1995, PASP, 107, 375
Onorato, S., Hennawi, J. F., Schindler, J.-T., et al. 2025, MNRAS, 540, 1308
Onorato, S., Hennawi, J. F., Pizzati, E., Venemans, B. P., & Eilers, A.-C. 2026, MNRAS, 547, stag388
Onoue, M., Ding, X., Silverman, J. D., et al. 2025, Nat. Astron., 9, 1541
Pasha, I., & Miller, T. B. 2023, J. Open Source Softw., 8, 5703
Perger, K., Fogasy, J., Frey, S., & Gabányi, K. É. 2025, A&A, 693, L2
Pizzati, E., Hennawi, J. F., Schaye, J., et al. 2024, MNRAS, 534, 3155
Pizzati, E., Hennawi, J. F., Schaye, J., et al. 2025, MNRAS, 539, 2910
Planck Collaboration VI. 2020, A&A, 641, A6
Pogge, R. W., Atwood, B., Brewer, D. F., et al. 2010, SPIE Conf. Ser., 7735, 77350A
Prochaska, J., Hennawi, J., Westfall, K., et al. 2020, J. Open Source Softw., 5, 2308
Roberts-Borsani, G., Treu, T., Shapley, A., et al. 2024, ApJ, 976, 193
Roberts-Borsani, G., Bagley, M., Rojas-Ruiz, S., et al. 2025, ApJ, 983, 18
Runnoe, J. C., Brotherton, M. S., & Shang, Z. 2012, MNRAS, 422, 478
Salvato, M., Wolf, J., Dwelly, T., et al. 2022, A&A, 661, A3
Schindler, J.-T. 2022, Astrophysics Source Code Library [record ascl:2202.018]
Schindler, J.-T., Farina, E. P., Bañados, E., et al. 2020, ApJ, 905, 51
Schindler, J.-T., Hennawi, J. F., Davies, F. B., et al. 2025, Nat. Astron., 9, 1732
Seifert, W., Appenzeller, I., Baumeister, H., et al. 2003, SPIE Conf. Ser., 4841, 962
Shen, Y., Wu, J., Jiang, L., et al. 2019, ApJ, 873, 35
Shibuya, T., Ouchi, M., & Harikane, Y. 2015, ApJS, 219, 15
Shimwell, T. W., Hardcastle, M. J., Tasse, C., et al. 2022, A&A, 659, A1
Silverman, J. D., Li, J., Ding, X., et al. 2025, ApJ, 995, L67
Simcoe, R. A., Burgasser, A. J., Bochanski, J. J., et al. 2010, SPIE Conf. Ser., 7735, 773514
Sobral, D., Matthee, J., Darvish, B., et al. 2015, ApJ, 808, 139
Sun, W., Ho, L. C., Zhuang, M.-Y., et al. 2024, ApJ, 960, 104
Tee, W. L., Fan, X., Wang, F., & Yang, J. 2025, ApJ, 983, L26
Telfer, R. C., Zheng, W., Kriss, G. A., & Davidsen, A. F. 2002, ApJ, 565, 773
Vestergaard, M., & Peterson, B. M. 2006, ApJ, 641, 689
Virtanen, P., Gommers, R., Oliphant, T. E., et al. 2020, Nat. Med., 17, 261
Wang, F., Yang, J., Fan, X., et al. 2018, ApJ, 869, L9
Wang, F., Yang, J., Fan, X., et al. 2021, ApJ, 907, L1
Wang, F., Yang, J., Hennawi, J. F., et al. 2023, ApJ, 951, L4
Wang, F., Yang, J., Fan, X., et al. 2024, ApJ, 968, 9
Willott, C. J., Delorme, P., Reylé, C., et al. 2010, AJ, 139, 906
Willott, C. J., Bergeron, J., & Omont, A. 2017, ApJ, 850, 108
Wolf, J., Salvato, M., Belladitta, S., et al. 2024, A&A, 691, A30
Yang, J., Wang, F., Fan, X., et al. 2020a, ApJ, 897, L14
Yang, J., Wang, F., Fan, X., et al. 2020b, ApJ, 904, 26
Yang, J., Wang, F., Fan, X., et al. 2021, ApJ, 923, 262
Yang, D.-M., Schindler, J.-T., Nanni, R., et al. 2024, MNRAS, 528, 2679
Yue, M., Eilers, A.-C., Ananna, T. T., et al. 2024, ApJ, 974, L26
Zonca, A., Singer, L., Lenz, D., et al. 2020, Astrophysics Source Code Library [record ascl:2008.022]

[1] Leiden Observatory, Leiden University, Einsteinweg 55, 2333 CC Leiden, The Netherlands
[2] Department of Physics, University of California, Santa Barbara, CA 93106, USA
[3] Hamburger Sternwarte, University of Hamburg, Gojenbergsweg 112, 21029 Hamburg, Germany
[4] INAF-Osservatorio Astronomico di Trieste, Via G. B. Tiepolo 11, 34143 Trieste, Italy
[5] Max-Planck-Institut für Astronomie, Königstuhl 17, 69117 Heidelberg, Germany
[6] INAF-Osservatorio di Astrofisica e Scienza dello Spazio di Bologna, Via Piero Gobetti 93/3, 40129 Bologna, Italy
[7] Astrophysics Group, Blackett Laboratory, Imperial College London, London SW7 2AZ, UK
[8] Department of Mathematics, Imperial College London, London SW7 2AZ, UK
[9] Department of Astronomy, University of Michigan, 1085 S. University Ave., Ann Arbor, MI 48109, USA
[10] Steward Observatory, University of Arizona, 933 N. Cherry Ave, Tucson, AZ 85750, USA
[11] Jet Propulsion Laboratory, California Institute of Technology, 4800 Oak Grove Drive, Pasadena, CA 91109, USA
[12] Herzberg Astronomy and Astrophysics Research Centre, 5071 W. Saanich Rd., Victoria, BC V9E 2E7, Canada
[13] Department of Physics & Astronomy, University of California Irvine, Irvine, CA 92697, USA
[14] Department of Physics, Oxford University, Keble Road, Oxford OX1 3RH, UK
[15] Department of Physics, Massachusetts Institute of Technology, Cambridge, MA 02139, USA
[16] MIT Kavli Institute for Astrophysics and Space Research, Massachusetts Institute of Technology, Cambridge, MA 02139, USA
[17] Aix-Marseille Université, CNRS, CNES, LAM, Marseille, France
[18] Kapteyn Astronomical Institute, University of Groningen, PO Box 800, 9700 AV Groningen, The Netherlands
[19] Department of Astronomy/Steward Observatory, University of Arizona, 933 N. Cherry Avenue, Tucson, AZ 85721, USA

[20] Instituto de Astrofísica, Facultad de Física, Pontificia Universidad Católica de Chile Av. Vicuña Mackenna 4860, 7820436 Macul, Santiago, Chile
[21] Fakultät für Physik und Astronomie, Universität Heidelberg Im Neuenheimer Feld 226, 69115 Heidelberg, Germany
[22] Research Center for Space and Cosmic Evolution, Ehime University, 2-5 Bunkyo-cho, Matsuyama, Ehime 790-8577, Japan
[23] Waseda Institute for Advanced Study (WIAS), Waseda University, 1-21-1, Nishi-Waseda, Shinjuku, Tokyo 169-0051, Japan
[24] Kavli Institute for the Physics and Mathematics of the Universe (WPI), University of Tokyo, Kashiwa, Chiba 277-8583, Japan
[25] Department of Astronomy and Astrophysics, 525 Davey Lab, The Pennsylvania State University, University Park, PA 16802, USA
[26] INAF-IASF Milano, Via Alfonso Corti 12, 20133 Milano, Italy
[27] Department of Astronomy, Tsinghua University, Beijing 100084, China
[28] Institut d'Astrophysique de Paris, UMR 7095, CNRS, and Sorbonne Université, 98 bis boulevard Arago, 75014 Paris, France
[29] Institut für Theoretische Physik, University of Heidelberg, Philosophenweg 16, 69120 Heidelberg, Germany
[30] Jodrell Bank Centre for Astrophysics, Department of Physics and Astronomy, University of Manchester, Oxford Road, Manchester M13 9PL, UK
[31] Instituto de Astrofísica de Canarias, E-38205 La Laguna, Tenerife, Spain
[32] Universidad de La Laguna, Dpto. Astrofísica, E-38206 La Laguna, Tenerife, Spain
[33] Institute for Cosmic Ray Research, The University of Tokyo, 5-1-5 Kashiwanoha, Kashiwa, Chiba 277-8582, Japan
[34] Institute of Theoretical Astrophysics, University of Oslo, P.O. Box 1029, Blindern 0315, Oslo, Norway
[35] Kavli Institute for Cosmology Cambridge, Madingley Road, Cambridge CB3 0HA, UK
[36] Institute of Astronomy, University of Cambridge, Madingley Road, Cambridge CB3 0HA, UK
[37] INAF-Istituto di Astrofisica e Planetologia Spaziali, Via del Fosso del Cavaliere, 100, 00100 Roma, Italy
[38] Institute of Science and Technology Austria (ISTA), Am Campus 1, 3400 Klosterneuburg, Austria
[39] Department of Mathematics and Physics, Roma Tre University, Via della Vasca Navale 84, 00146 Rome, Italy
[40] INAF-Osservatorio Astronomico di Roma, Via Frascati 33, 00078 Monteporzio Catone, Italy
[41] Dipartimento di Fisica e Astronomia, Università di Firenze, Via G. Sansone 1, 50019 Sesto Fiorentino, Firenze, Italy
[42] University of Trento, Via Sommarive 14, I-38123 Trento, Italy
[43] INAF-Osservatorio Astrofisico di Arcetri, Largo E. Fermi 5, 50125 Firenze, Italy
[44] Department of Physics and Astronomy, University of British Columbia, Vancouver BC V6T 1Z1, Canada
[45] Institute for Particle Physics and Astrophysics, Dept. of Physics, ETH Zurich, Wolfgang-Pauli-Strasse 27, 8093 Zurich, Switzerland
[46] Department of Astronomy, University of Geneva, ch. d'Ecogia 16, 1290 Versoix, Switzerland
[47] Department of Physical Sciences, Ritsumeikan University, Kusatsu, Shiga 525-8577, Japan
[48] Academia Sinica Institute of Astronomy and Astrophysics (ASIAA), 11F of ASMAB, No. 1, Section 4, Roosevelt Road, Taipei 10617, Taiwan
[49] ESAC/ESA, Camino Bajo del Castillo, s/n., Urb. Villafranca del Castillo, 28692 Villanueva de la Cañada, Madrid, Spain
[50] School of Mathematics and Physics, University of Surrey, Guildford, Surrey GU2 7XH, UK
[51] INAF-Osservatorio Astronomico di Brera, Via Brera 28, 20122 Milano, Italy
[52] Université Paris-Saclay, Université Paris Cité, CEA, CNRS, AIM, 91191 Gif-sur-Yvette, France
[53] IFPU, Institute for Fundamental Physics of the Universe, Via Beirut 2, 34151 Trieste, Italy
[54] INFN, Sezione di Trieste, Via Valerio 2, 34127 Trieste, TS, Italy
[55] SISSA, International School for Advanced Studies, Via Bonomea 265, 34136 Trieste, TS, Italy
[56] Dipartimento di Fisica e Astronomia, Università di Bologna, Via Gobetti 93/2, 40129 Bologna, Italy
[57] INFN-Sezione di Bologna, Viale Berti Pichat 6/2, 40127 Bologna, Italy
[58] INAF-Osservatorio Astronomico di Padova, Via dell'Osservatorio 5, 35122 Padova, Italy
[59] Dipartimento di Fisica, Università di Genova, Via Dodecaneso 33, 16146 Genova, Italy
[60] INFN-Sezione di Genova, Via Dodecaneso 33, 16146 Genova, Italy
[61] Department of Physics "E. Pancini", University Federico II, Via Cinthia 6, 80126 Napoli, Italy
[62] INAF-Osservatorio Astronomico di Capodimonte, Via Moiariello 16, 80131 Napoli, Italy
[63] Dipartimento di Fisica, Università degli Studi di Torino, Via P. Giuria 1, 10125 Torino, Italy
[64] INFN-Sezione di Torino, Via P. Giuria 1, 10125 Torino, Italy
[65] INAF-Osservatorio Astrofisico di Torino, Via Osservatorio 20, 10025 Pino Torinese (TO), Italy
[66] Institute for Astronomy, University of Edinburgh, Royal Observatory, Blackford Hill, Edinburgh EH9 3HJ, UK
[67] Centro de Investigaciones Energéticas, Medioambientales y Tecnológicas (CIEMAT), Avenida Complutense 40, 28040 Madrid, Spain
[68] Port d'Informació Científica, Campus UAB, C. Albareda s/n, 08193 Bellaterra (Barcelona), Spain
[69] INFN section of Naples, Via Cinthia 6, 80126 Napoli, Italy
[70] Institute for Astronomy, University of Hawaii, 2680 Woodlawn Drive, Honolulu, HI 96822, USA
[71] Dipartimento di Fisica e Astronomia "Augusto Righi" – Alma Mater Studiorum Università di Bologna, Viale Berti Pichat 6/2, 40127 Bologna, Italy
[72] European Space Agency/ESRIN, Largo Galileo Galilei 1, 00044 Frascati, Roma, Italy
[73] Université Claude Bernard Lyon 1, CNRS/IN2P3, IP2I Lyon, UMR 5822, Villeurbanne F-69100, France
[74] Institut de Ciències del Cosmos (ICCUB), Universitat de Barcelona (IEEC-UB), Martí i Franquès 1, 08028 Barcelona, Spain
[75] Institució Catalana de Recerca i Estudis Avançats (ICREA), Passeig de Lluís Companys 23, 08010 Barcelona, Spain
[76] Institut de Ciencies de l'Espai (IEEC-CSIC), Campus UAB, Carrer de Can Magrans, s/n Cerdanyola del Vallés, 08193 Barcelona, Spain
[77] UCB Lyon 1, CNRS/IN2P3, IUF, IP2I Lyon, 4 rue Enrico Fermi, 69622 Villeurbanne, France
[78] Mullard Space Science Laboratory, University College London, Holmbury St Mary, Dorking, Surrey RH5 6NT, UK
[79] Université Paris-Saclay, CNRS, Institut d'astrophysique spatiale, 91405 Orsay, France
[80] INFN-Padova, Via Marzolo 8, 35131 Padova, Italy
[81] Aix-Marseille Université, CNRS/IN2P3, CPPM, Marseille, France
[82] INFN-Bologna, Via Irnerio 46, 40126 Bologna, Italy
[83] University Observatory, LMU Faculty of Physics, Scheinerstr. 1, 81679 Munich, Germany
[84] FRACTAL S.L.N.E., calle Tulipán 2, Portal 13 1A, 28231 Las Rozas de Madrid, Spain
[85] Max Planck Institute for Extraterrestrial Physics, Giessenbachstr. 1, 85748 Garching, Germany
[86] Universitäts-Sternwarte München, Fakultät für Physik, Ludwig-Maximilians-Universität München, Scheinerstr. 1, 81679 München, Germany
[87] Dipartimento di Fisica "Aldo Pontremoli", Università degli Studi di Milano, Via Celoria 16, 20133 Milano, Italy
[88] INFN-Sezione di Milano, Via Celoria 16, 20133 Milano, Italy
[89] Department of Physics, Lancaster University, Lancaster LA1 4YB, UK

[90] Felix Hormuth Engineering, Goethestr. 17, 69181 Leimen, Germany
[91] Technical University of Denmark, Elektrovej 327, 2800 Kgs. Lyngby, Denmark
[92] Cosmic Dawn Center (DAWN), Denmark
[93] NASA Goddard Space Flight Center, Greenbelt, MD 20771, USA
[94] Université de Genève, Département de Physique Théorique and Centre for Astroparticle Physics, 24 quai Ernest-Ansermet, CH-1211 Genève 4, Switzerland
[95] Department of Physics, P.O. Box 64, University of Helsinki 00014, Helsinki, Finland
[96] Helsinki Institute of Physics, Gustaf Hällströmin katu 2, University of Helsinki, 00014 Helsinki, Finland
[97] Laboratoire d'etude de l'Univers et des phenomenes eXtremes, Observatoire de Paris, Université PSL, Sorbonne Université, CNRS, 92190 Meudon, France
[98] SKAO, Jodrell Bank, Lower Withington, Macclesfield SK11 9FT, UK
[99] Centre de Calcul de l'IN2P3/CNRS, 21 avenue Pierre de Coubertin, 69627 Villeurbanne Cedex, France
[100] Universität Bonn, Argelander-Institut für Astronomie, Auf dem Hügel 71, 53121 Bonn, Germany
[101] INFN-Sezione di Roma, Piazzale Aldo Moro, 2 – c/o Dipartimento di Fisica, Edificio G. Marconi, 00185 Roma, Italy
[102] Dipartimento di Fisica e Astronomia "Augusto Righi" – Alma Mater Studiorum Università di Bologna, Via Piero Gobetti 93/2, 40129 Bologna, Italy
[103] Department of Physics, Institute for Computational Cosmology, Durham University, South Road, Durham DH1 3LE, UK
[104] Université Paris Cité, CNRS, Astroparticule et Cosmologie, 75013 Paris, France
[105] CNRS-UCB International Research Laboratory, Centre Pierre Binétruy, IRL2007, CPB-IN2P3, Berkeley, USA
[106] Institut d'Astrophysique de Paris, 98bis Boulevard Arago, 75014 Paris, France
[107] Institute of Physics, Laboratory of Astrophysics, Ecole Polytechnique Fédérale de Lausanne (EPFL), Observatoire de Sauverny, 1290 Versoix, Switzerland
[108] Telespazio UK S.L. for European Space Agency (ESA), Camino bajo del Castillo, s/n, Urbanizacion Villafranca del Castillo, Villanueva de la Cañada 28692, Madrid, Spain
[109] Institut de Física d'Altes Energies (IFAE), The Barcelona Institute of Science and Technology, Campus UAB, 08193 Bellaterra (Barcelona), Spain
[110] European Space Agency/ESTEC, Keplerlaan 1, 2201 AZ Noordwijk, The Netherlands
[111] DARK, Niels Bohr Institute, University of Copenhagen, Jagtvej 155, 2200 Copenhagen, Denmark
[112] Waterloo Centre for Astrophysics, University of Waterloo, Waterloo, Ontario N2L 3G1, Canada
[113] Department of Physics and Astronomy, University of Waterloo, Waterloo, Ontario N2L 3G1, Canada
[114] Perimeter Institute for Theoretical Physics, Waterloo, Ontario N2L 2Y5, Canada
[115] Space Science Data Center, Italian Space Agency, Via del Politecnico snc, 00133 Roma, Italy
[116] Centre National d'Etudes Spatiales – Centre spatial de Toulouse, 18 avenue Edouard Belin, 31401 Toulouse Cedex 9, France
[117] Institute of Space Science, Str. Atomistilor, nr. 409 Măgurele, Ilfov 077125, Romania
[118] Consejo Superior de Investigaciones Cientificas, Calle Serrano 117, 28006 Madrid, Spain
[119] Dipartimento di Fisica e Astronomia "G. Galilei", Università di Padova, Via Marzolo 8, 35131 Padova, Italy
[120] Caltech/IPAC, 1200 E. California Blvd., Pasadena, CA 91125, USA
[121] Institut de Recherche en Astrophysique et Planétologie (IRAP), Université de Toulouse, CNRS, UPS, CNES, 14 Av. Edouard Belin, 31400 Toulouse, France
[122] Université St Joseph; Faculty of Sciences, Beirut, Lebanon
[123] Departamento de Física, FCFM, Universidad de Chile, Blanco Encalada, 2008 Santiago, Chile
[124] Universität Innsbruck, Institut für Astro- und Teilchenphysik, Technikerstr. 25/8, 6020 Innsbruck, Austria
[125] Institut d'Estudis Espacials de Catalunya (IEEC), Edifici RDIT, Campus UPC, 08860 Castelldefels, Barcelona, Spain
[126] Satlantis, University Science Park, Sede Bld 48940, Leioa-Bilbao, Spain
[127] Institute of Space Sciences (ICE, CSIC), Campus UAB, Carrer de Can Magrans, s/n, 08193 Barcelona, Spain
[128] Department of Physics and Helsinki Institute of Physics, Gustaf Hällströmin katu 2, University of Helsinki, 00014 Helsinki, Finland
[129] Departamento de Física, Faculdade de Ciências, Universidade de Lisboa, Edifício C8, Campo Grande, PT1749-016 Lisboa, Portugal
[130] Instituto de Astrofísica e Ciências do Espaço, Faculdade de Ciências, Universidade de Lisboa, Tapada da Ajuda, 1349-018 Lisboa, Portugal
[131] Cosmic Dawn Center (DAWN)
[132] Niels Bohr Institute, University of Copenhagen, Jagtvej 128, 2200 Copenhagen, Denmark
[133] Universidad Politécnica de Cartagena, Departamento de Electrónica y Tecnología de Computadoras, Plaza del Hospital 1, 30202 Cartagena, Spain
[134] Université PSL, Observatoire de Paris, Sorbonne Université, CNRS, LERMA, 75014 Paris, France
[135] Université Paris-Cité, 5 Rue Thomas Mann, 75013 Paris, France
[136] Aurora Technology for European Space Agency (ESA), Camino bajo del Castillo, s/n, Urbanizacion Villafranca del Castillo, Villanueva de la Cañada 28692, Madrid, Spain
[137] Dipartimento di Fisica – Sezione di Astronomia, Università di Trieste, Via Tiepolo 11, 34131 Trieste, Italy
[138] ICL, Junia, Université Catholique de Lille, LITL, 59000 Lille, France
[139] ICSC – Centro Nazionale di Ricerca in High Performance Computing, Big Data e Quantum Computing, Via Magnanelli 2, Bologna, Italy

Appendix A: Discovery observations and new quasar properties

Table A.1. Journal of discovery observations.

Target	Telescope	Instrument	Exposure (s)	Date (UTC)	Program ID
EUCL J150537.32+773441.0	Keck	LRIS	1200	2024-07-01	U259
EUCL J141841.29+694930.6	Keck	LRIS	2400	2024-07-01	U259
	Keck	KCWI	2400	2025-01-21	U267
EUCL J125308.55+705432.3	Keck	LRIS	1200	2024-07-01[a]	U259
	Keck	MOSFIRE	3900	2024-12-30[b]	U418
	Keck	MOSFIRE	4200	2025-01-08	U418
EUCL J144545.82+714342.3	Keck	LRIS	1200	2024-07-02[a]	U259
	Keck	KCWI	2400	2025-01-24[a]	U267
	Keck	MOSFIRE	3000	2025-01-25	U418
EUCL J143448.06+685733.2	Keck	LRIS	2400	2024-07-03	U259
EUCL J115522.89+704612.3	Keck	LRIS	3600	2024-07-03	U259
EUCL J031547.94−684405.6	Magellan	FIRE	1800	2024-11-16	
EUCL J025210.37−412533.8	Magellan	FIRE	1800	2024-11-16	
EUCL J025029.93−531706.7	Magellan	FIRE	1800	2024-11-16	
EUCL J041250.73−563949.7	Magellan	FIRE	1800	2024-11-16	
	Magellan	FIRE	1800	2024-12-20[a],[c]	
	Magellan	FIRE	3600	2025-03-16[b]	
EUCL J045148.19−342622.2	Magellan	FIRE	1800	2024-11-17	
EUCL J052645.38−460902.7	Magellan	FIRE	1800	2024-11-17	
EUCL J050240.93−384906.1	Magellan	FIRE	1800	2024-11-17	
EUCL J052209.82−512709.2[d]	Magellan	FIRE	3600	2024-11-18	
EUCL J044326.27−533214.9	Magellan	FIRE	1800	2024-12-20	
EUCL J091639.93+683652.9	Keck	KCWI	1200	2024-12-23	U267
EUCL J093330.60+742730.0	Keck	KCWI	1200	2024-12-23	U267
EUCL J135534.55+700055.5	Keck	KCWI	5100	2024-12-23[b]	U267
	Keck	MOSFIRE	3300	2024-12-29	U418
EUCL J134031.50+674715.1	Keck	KCWI	1200	2024-12-23[c]	U267
	Keck	KCWI	1200	2025-01-24	U267
EUCL J173243.48+601612.6	Keck	KCWI	600	2025-01-22[b]	U267
EUCL J101255.87+663058.0	Keck	KCWI	1800	2025-01-22[a]	U267
	Keck	MOSFIRE	2400	2025-06-16	U275
	Keck	MOSFIRE	5400	2025-06-17	U275
EUCL J172258.31+574133.5	Keck	KCWI	900	2025-01-23[a],[c]	U267
	Keck	KCWI	2100	2025-01-24[b]	U267
	Keck	MOSFIRE	1200	2025-01-25[b]	U267
	Keck	KCWI	1800	2025-01-28	U267
	Keck	KCWI	3600	2025-06-18	U275

Notes. All dates are given in Coordinated Universal Time (UTC). The list follows the chronological order of the first observation of each quasar.
[a] No detection in this observation.
[b] Some exposures were taken in twilight.
[c] Cloudy conditions, corresponding to > 0.5 mag of extinction, or poor seeing, corresponding to > 1.″5.
[d] An echelle-mode observation was conducted for this target.

Table A.2. Journal of discovery observations continued.

Target	Telescope	Instrument	Exposure (s)	Date (UTC)	Program ID
EUCL J044657.86−570046.6	Magellan	FIRE	1800	2025-03-16	
EUCL J181159.50+614554.2	Keck	KCWI	900	2025-06-18	U275
EUCL J163141.37+625920.6	Keck	MOSFIRE	3900	2025-07-18	N110
EUCL J172902.75+641018.1	Keck	MOSFIRE	8100	2025-08-17[b]	U262
	LBT	LUCI	10080	2025-09-24	
EUCL J161430.31+452847.1	Keck	KCWI	2400	2025-08-28	U262
EUCL J155552.09+515258.7	Keck	MOSFIRE	3600	2025-07-22	N110
	Keck	KCWI	1200	2025-08-28	U262
EUCL J170707.89+650252.7	Keck	MOSFIRE	3600	2025-07-17[a,b]	N110
	Keck	MOSFIRE	3600	2025-07-18	N110
	Keck	KCWI	600	2025-08-28	U262
EUCL J154359.34+471810.4	Keck	MOSFIRE	3000	2025-08-17[b]	U262
	Keck	KCWI	1200	2025-08-29	U262
EUCL J153722.76+582927.2	Keck	MOSFIRE	1200	2025-07-23	N110
	Keck	KCWI	1200	2025-08-28	U262

Notes. All dates are given in Coordinated Universal Time (UTC). This table continues Table A.1.
[a] No detection in this observation.
[b] Cloudy conditions, corresponding to > 0.5 mag of extinction, and/or poor seeing, corresponding to > 1.″5.

Table A.3. Properties of the newly discovered quasars.

Name	RA (J2000)	Dec (J2000)	Redshift	I_E	z^a	Y_E	J_E	H_E	M_{1450}	$\log(L_{bol}/L_\odot)$
EUCL J172902.75+641018.1	17:29:02.75	+64:10:18.1	7.77	> 28.28	...	22.61 ± 0.04	22.02 ± 0.03	21.97 ± 0.03	–25.05	46.45
EUCL J125308.55+705432.3	12:53:08.55	+70:54:32.3	7.69	> 28.57	> 24.91	23.56 ± 0.09	22.97 ± 0.07	22.96 ± 0.06	–24.06	46.10
EUCL J101255.87+663058.0	10:12:55.87	+66:30:58.0	7.61	> 28.40	> 24.67	23.50 ± 0.11	23.00 ± 0.09	22.93 ± 0.07	–23.98	46.07
EUCL J052209.82−512709.2	05:22:09.82	−51:27:09.2	7.50	> 28.31	> 24.47	22.54 ± 0.05	22.17[b]	22.19 ± 0.04	–24.75	46.35
EUCL J135534.55+700055.5	13:55:34.55	+70:00:55.5	7.45	> 28.55	> 24.66	22.17 ± 0.03	21.89 ± 0.03	21.78 ± 0.03	–25.01	46.44
EUCL J144545.82+714342.3	14:45:45.82	+71:43:42.3	7.36	> 28.52	> 24.86	23.13 ± 0.09	22.78 ± 0.06	22.55 ± 0.06	–24.10	46.11
EUCL J141841.29+694930.6	14:18:41.29	+69:49:30.6	7.35	> 28.64	> 24.91	23.47 ± 0.08	22.88 ± 0.04	22.61 ± 0.05	–24.00	46.07
EUCL J163141.37+625920.6	16:31:41.37	+62:59:20.6	7.33	> 28.22	> 24.63	22.54 ± 0.04	22.19 ± 0.03	22.24 ± 0.03	–24.69	46.32
EUCL J041250.73−563949.7	04:12:50.73	−56:39:49.7	7.17[c]	> 27.37	> 24.33	22.75 ± 0.05	22.42 ± 0.03	22.18 ± 0.03	–24.41	46.22
EUCL J134031.51+674715.0	13:40:31.51	+67:47:15.0	7.05	> 28.02	> 24.96	23.28 ± 0.14	23.12 ± 0.10	22.92 ± 0.09	–23.67	45.95
EUCL J172258.31+574133.5	17:22:58.31	+57:41:33.5	7.01	> 28.49	> 24.73	23.25 ± 0.07	22.84 ± 0.05	22.68 ± 0.05	–23.93	46.05
EUCL J161430.31+452847.1	16:14:30.31	+45:28:47.1	7.00	> 28.31	...	23.30 ± 0.08	22.97 ± 0.08	22.70 ± 0.08	–23.80	46.00
EUCL J093330.60+742730.0	09:33:30.60	+74:27:30.0	6.96	> 28.44	> 23.21	22.01 ± 0.03	21.77 ± 0.03	21.78 ± 0.03	–24.98	46.43
EUCL J155552.09+515258.7	15:55:52.09	+51:52:58.7	6.95	> 28.32	...	22.30 ± 0.04	22.22 ± 0.04	22.26 ± 0.03	–24.53	46.27
EUCL J050240.93−384906.1	05:02:40.93	−38:49:06.1	6.90	> 27.73	22.90 ± 0.08	21.53 ± 0.03	21.27 ± 0.02	21.24 ± 0.02	–25.46	46.61
EUCL J052645.38−460902.7	05:26:45.38	−46:09:02.7	6.89	> 28.12	23.49 ± 0.13	21.76 ± 0.02	21.54 ± 0.02	21.43 ± 0.02	–25.19	46.51
EUCL J025029.93−531706.7	02:50:29.93	−53:17:06.7	6.86	> 27.94	23.42 ± 0.15	21.81 ± 0.03	21.55 ± 0.02	21.49 ± 0.02	–25.17	46.50
EUCL J170707.89+650252.7	17:07:07.89	+65:02:52.7	6.84	> 28.42	> 24.98	22.56 ± 0.04	22.25 ± 0.03	22.28 ± 0.03	–24.46	46.24
EUCL J154359.34+471810.4	15:43:59.34	+47:18:10.4	6.84	> 28.07	...	22.63 ± 0.05	22.36 ± 0.04	22.30 ± 0.03	–24.35	46.20
EUCL J025210.37−412533.8	02:52:10.37	−41:25:33.8	6.83	> 27.98	23.19 ± 0.10	21.70 ± 0.03	21.39 ± 0.02	21.34 ± 0.02	–25.32	46.55
EUCL J143448.06+685733.2	14:34:48.06	+68:57:33.2	6.82	> 28.25	> 24.82	23.04 ± 0.06	23.04 ± 0.07	22.94 ± 0.06	–23.67	45.95
EUCL J150537.32+773441.0	15:05:37.32	+77:34:41.0	6.72	28.13 ± 0.34	> 24.36	22.20 ± 0.04	22.06 ± 0.03	22.19 ± 0.04	–24.52	46.26
EUCL J153722.76+582927.2	15:37:22.76	+58:29:27.2	6.68	> 28.29	...	23.14 ± 0.06	22.58 ± 0.04	22.43 ± 0.03	–24.10	46.11
EUCL J044326.27−533214.9	04:43:26.27	−53:32:14.9	6.67	> 28.20	23.60 ± 0.18	22.40 ± 0.03	22.22 ± 0.03	22.15 ± 0.02	–24.45	46.24
EUCL J045148.19−342622.2	04:51:48.19	−34:26:22.2	6.65	> 27.76	23.05 ± 0.10	22.18 ± 0.03	22.10 ± 0.03	22.11 ± 0.03	–24.57	46.28
EUCL J115522.89+704612.3	11:55:22.89	+70:46:12.3	6.65	> 28.48	> 24.70	23.39 ± 0.10	22.83 ± 0.06	22.60 ± 0.05	–23.84	46.02
EUCL J044657.86−570046.6	04:46:57.86	−57:00:46.6	6.64	> 28.03	24.46 ± 0.23	22.71 ± 0.05	22.48 ± 0.04	22.47 ± 0.05	–24.19	46.14
EUCL J091639.93+683652.9	09:16:39.93	+68:36:52.9	6.64	27.38 ± 0.13	23.55 ± 0.17	21.83 ± 0.03	21.73 ± 0.03	21.59 ± 0.03	–24.94	46.42
EUCL J181159.50+614554.2	18:11:59.50	+61:45:54.2	6.63	> 28.34	> 24.68	21.97 ± 0.05	22.07 ± 0.06	21.92 ± 0.04	–24.60	46.29
EUCL J173243.48+601612.6	17:32:43.48	+60:16:12.6	6.61	26.41 ± 0.05	23.88 ± 0.19	21.37 ± 0.04	21.30 ± 0.04	21.22 ± 0.03	–25.37	46.57
EUCL J031547.94−684405.6	03:15:47.94	−68:44:05.6	6.60	27.47 ± 0.27	...	21.69 ± 0.03	21.26 ± 0.02	20.97 ± 0.02	–25.42	46.59

Notes. The quasars are listed in order of decreasing redshift. Redshifts are estimated visually from the Lyα break, with typical uncertainties of 0.05–0.1 (e.g. Matsuoka et al. 2016, but see note c for cases where weak or absorbed Lyα increases the uncertainty to ~0.2). Broad-band magnitudes are derived from PSF-fitting photometry (Sect. 3.1); 3σ limits are reported for non-detections. The absolute magnitude M_{1450} is computed from the observed J_E-band magnitude assuming a spectral slope $\alpha = -1.7$ (e.g. Telfer et al. 2002), and the bolometric luminosity L_{bol} from the scaling relation of Runnoe et al. (2012).

[a] Entries marked with "..." indicate no ancillary z-band imaging is available at the source position.

[b] The J_E band photometry derived from the NIR stacked image is affected by hot pixels. Here we quote the magnitude measured from the JWST/NIRSpec spectrum of this target.

[c] The redshift is determined with the Mg II line in the JWST spectrum of this target.

Appendix B: Multi-band cutouts

Figures B.1 and B.2 display the 12″ × 12″ cutouts of I_E, z, Y_E, J_E, H_E bands of the new quasars reported in this work. These cutouts are available at https://doi.org/10.57780/esa-50769fd. The discovery spectra are available from the corresponding author upon reasonable request.

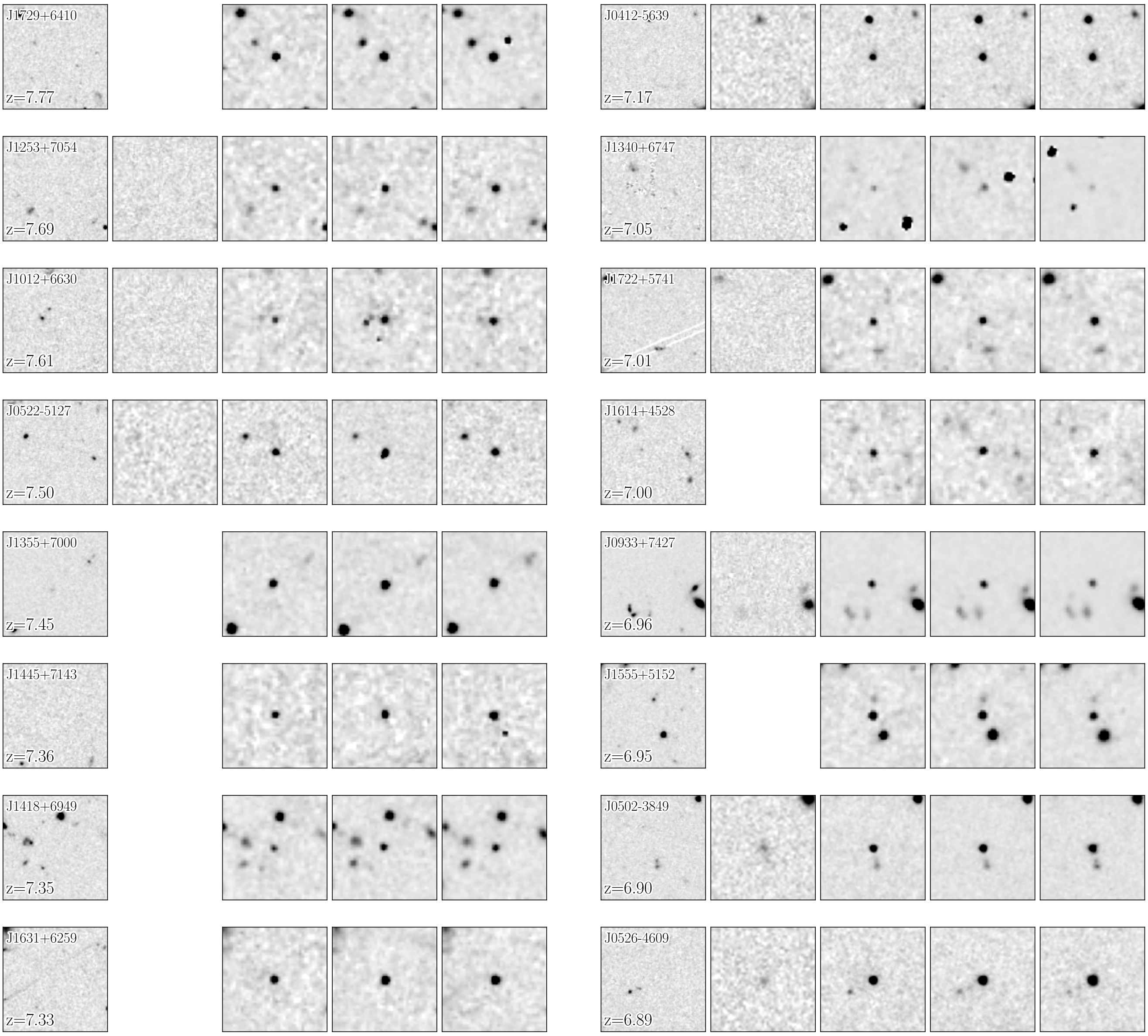

Fig. B.1. Cutouts of the new quasars (12″ × 12″) reported in this work. From left to right: I_E, z, Y_E, J_E, and H_E bands. Target names and their redshift are listed in the I_E-band cutouts.

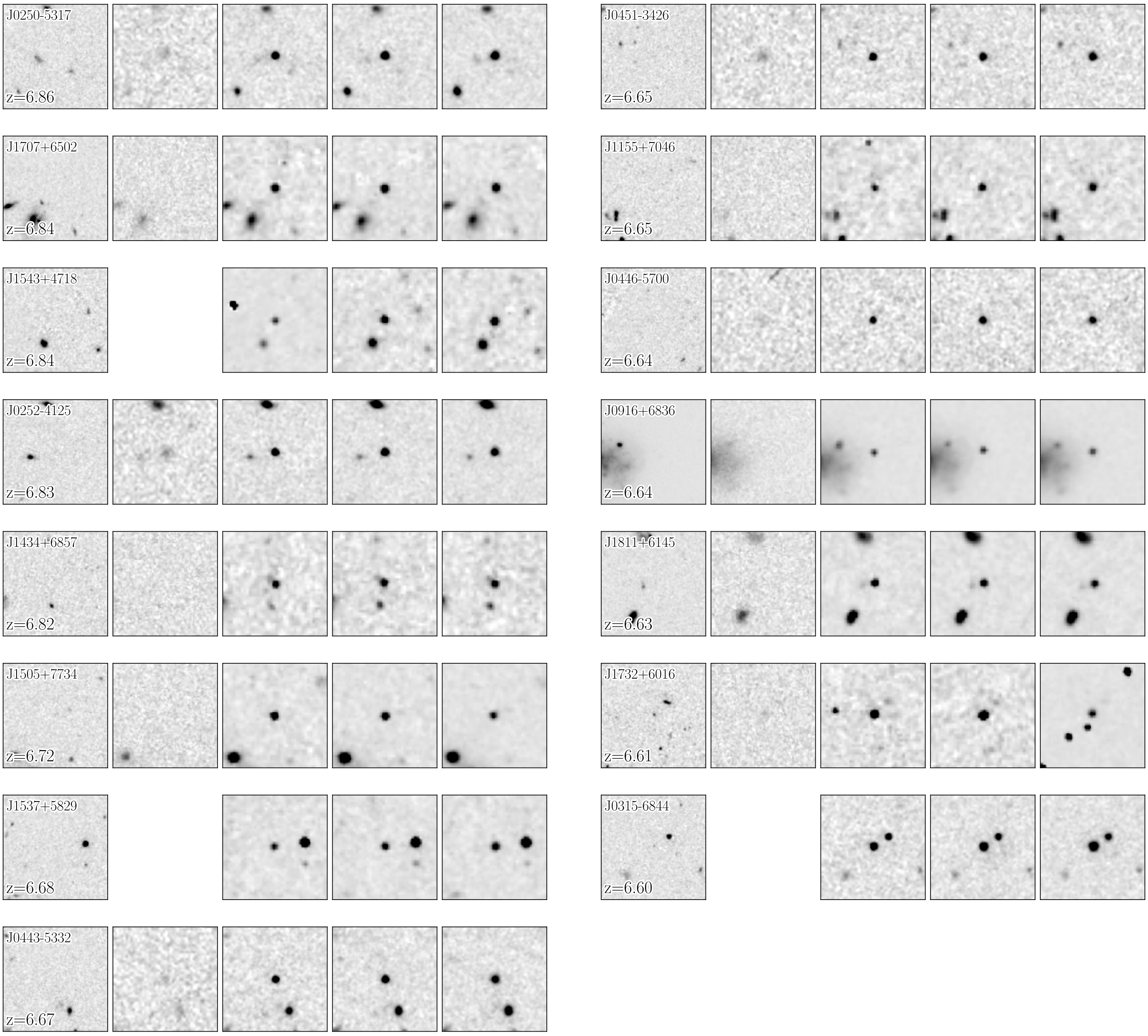

Fig. B.2. Same as Fig. B.1 but for the rest of the quasars.

Appendix C: Reduced 2D/1D discovery spectra

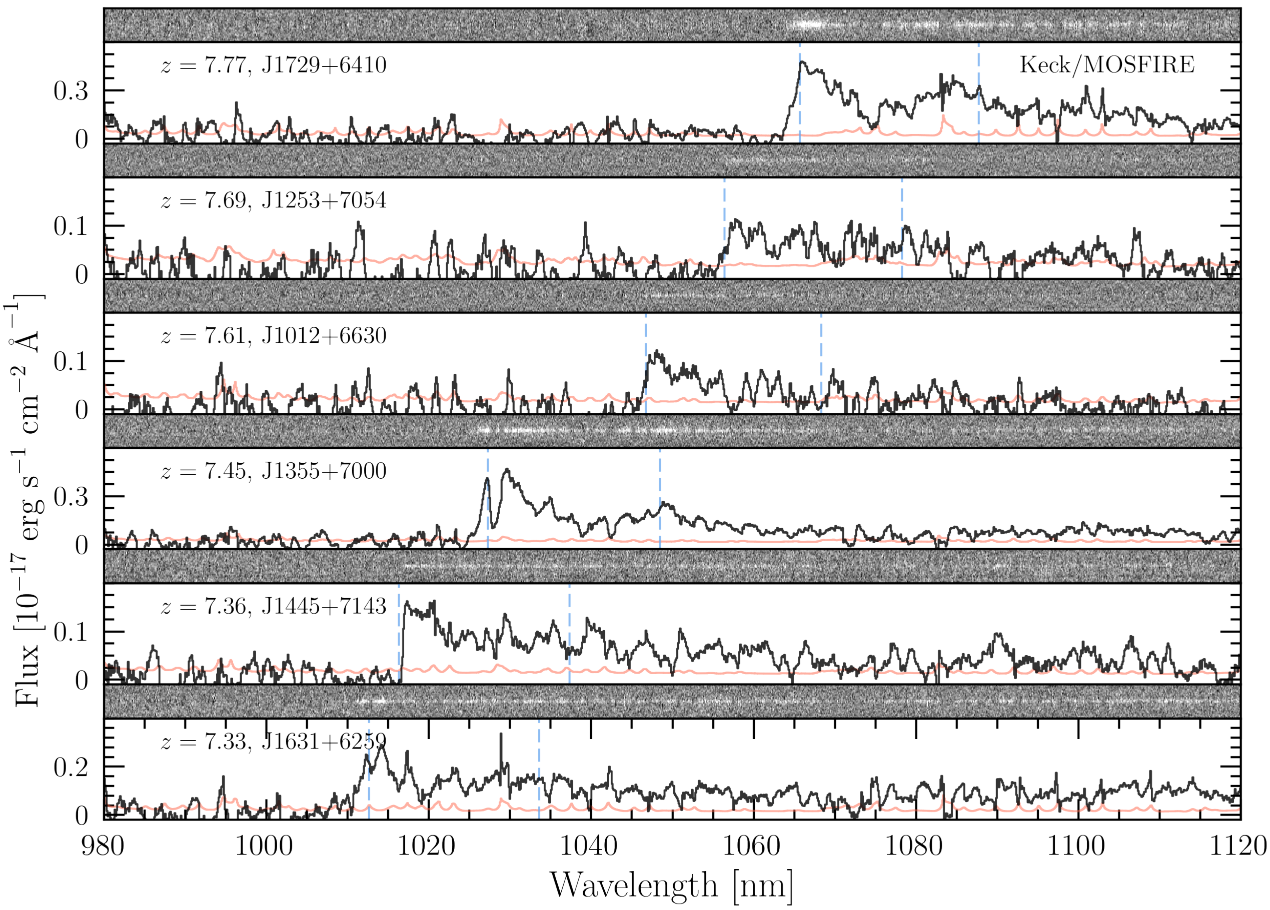

Fig. C.1. Reduced 2D/1D discovery spectra of Keck/MOSFIRE. The black curves are the fluxed spectra, smoothed with inverse-variance-weights with a boxcar of 9 pixel. The red curves are the noise vectors with the same smoothing. The light blue dashed lines mark the positions of the Lyα and N V lines at the tentative redshifts for each quasar. These redshifts are estimated from the Lyα lines.

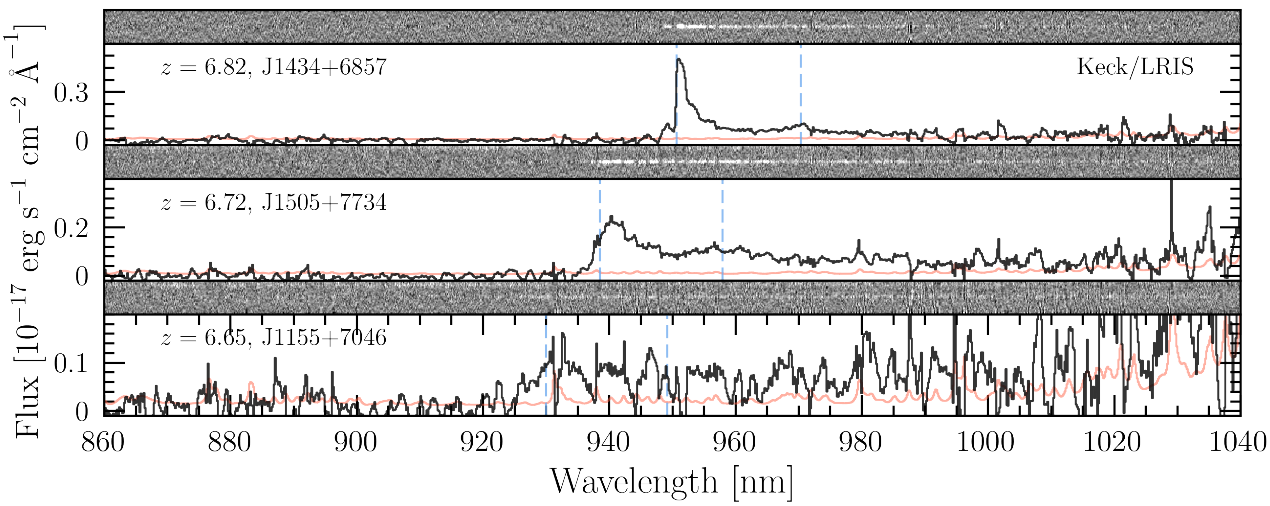

Fig. C.2. Reduced 2D/1D discovery spectra of Keck/LRIS. The spectra are inverse-variance-smoothed with a boxcar of 7 pixel.

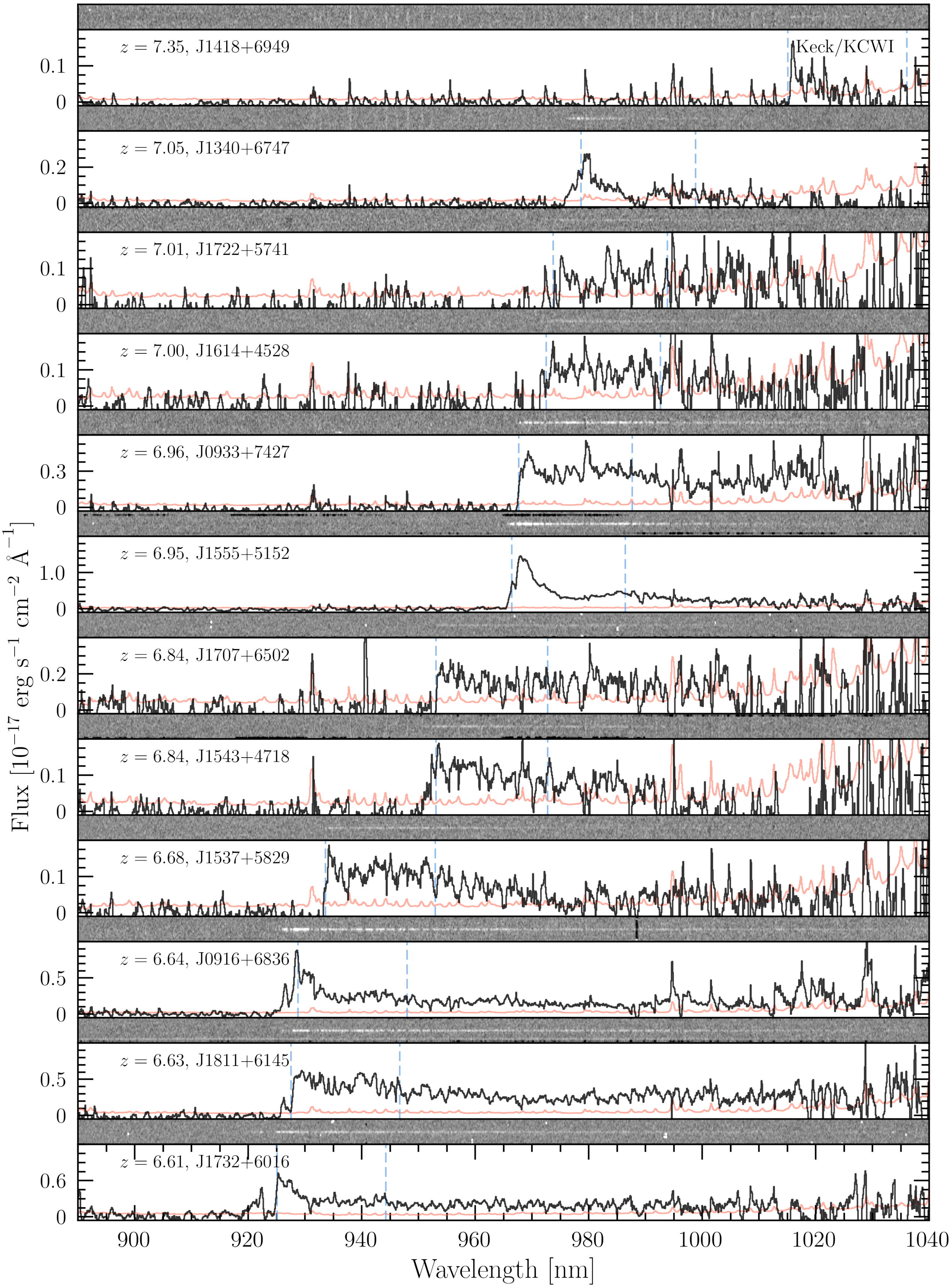

Fig. C.3. The reduced 2D and 1D discovery spectra of Keck/KCWI. The spectra are inverse-variance-smoothed with a boxcar of 7 pixel.

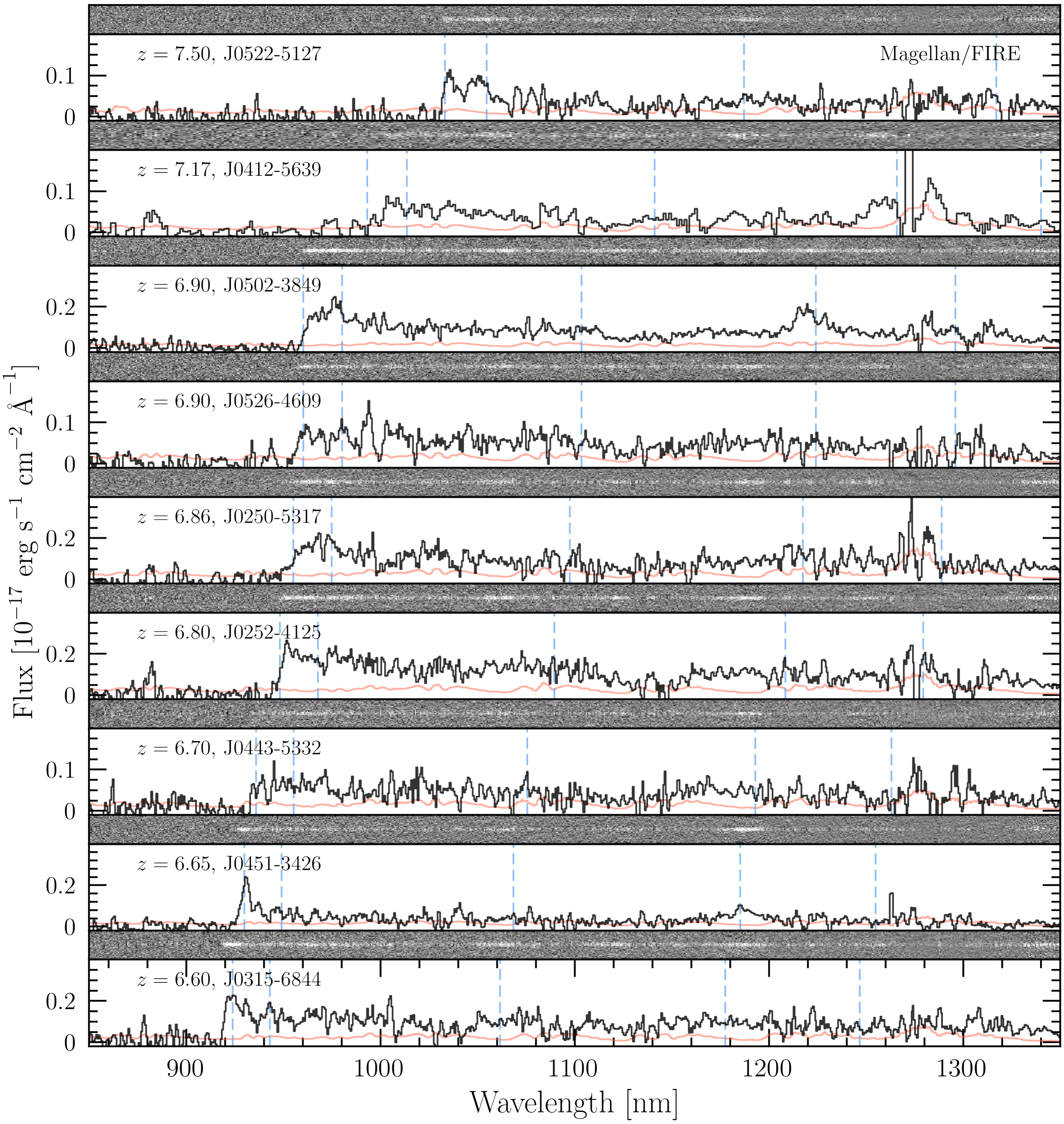

Fig. C.4. Reduced 2D/1D discovery spectra of Magellan/FIRE. The spectra are inverse-variance-smoothed with a boxcar of 3 pixel. The green dashed lines mark the positions of the Lyα, N V, Si IV, C IV, and He II lines at the tentative redshifts for each quasar. These redshifts are estimated from the Lyα lines.

Appendix D: Reduced 2D/1D spectra of some examples of contaminants

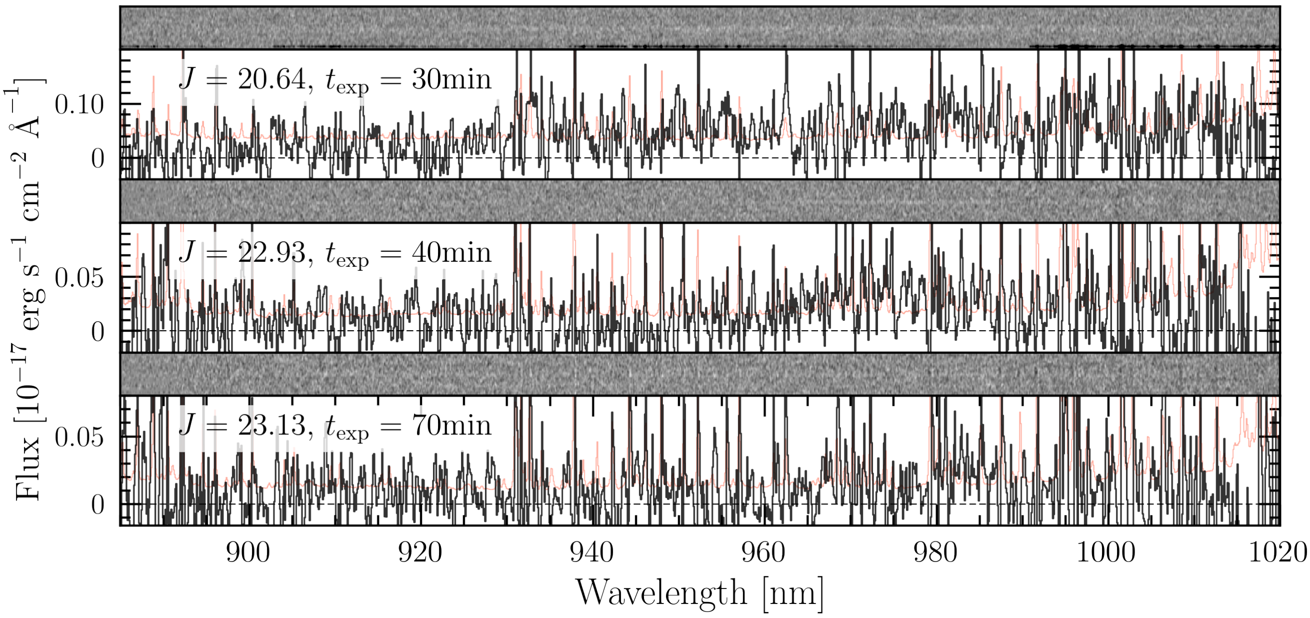

Fig. D.1. Reduced 2D/1D spectra of three contaminants observed with Keck/KCWI. The total exposure time and the $J_{\rm E}$-band magnitude for each target are listed in each panel. The black curves are the fluxed spectra, smoothed with an inverse-variance-weighting and a boxcar of 3 pixel. The red curves are the noise vectors with the same smoothing.

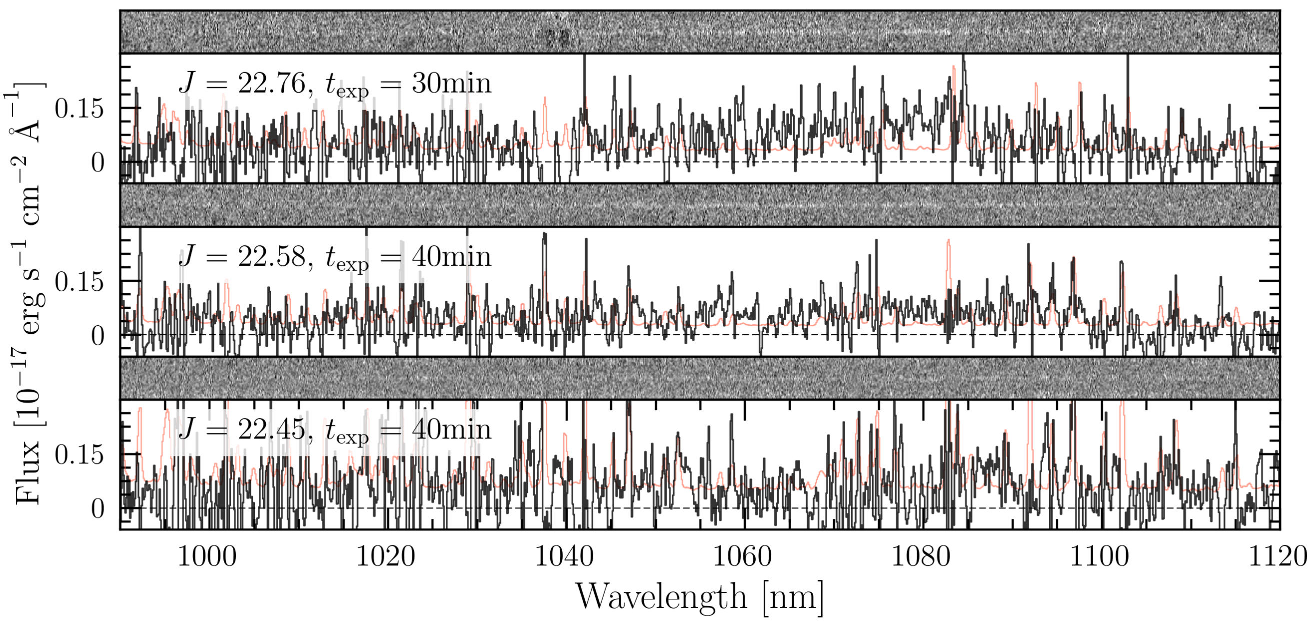

Fig. D.2. Same as Fig. D.1, but for Keck/MOSFIRE.

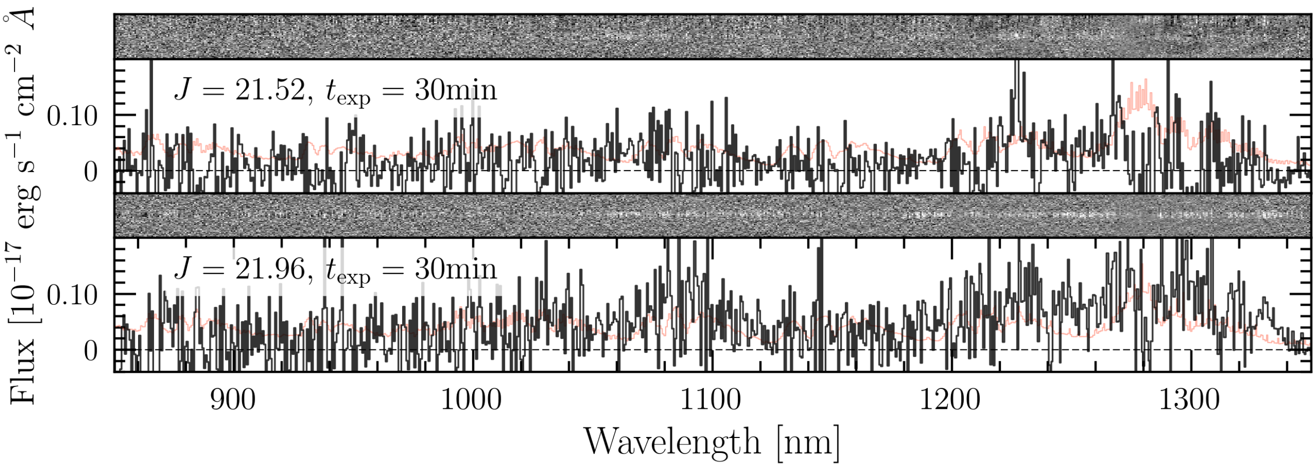

Fig. D.3. Same as Fig. D.1, but for Magellan/FIRE.

Table D.1. List of identified contaminants. Some of them were tentatively identified as brown dwarfs.

Name	RA	Dec	Instruments	Notes
EUCL J015220.18−632724.6	01:52:20.18	−63:27:24.6	FIRE	dwarf
EUCL J030218.49−535654.0	03:02:18.49	−53:56:54.0	FIRE	dwarf
EUCL J034256.06−541719.3	03:42:56.06	−54:17:19.3	FIRE	dwarf
EUCL J034303.88−552508.2	03:43:03.88	−55:25:08.2	FIRE	dwarf
EUCL J034343.36−544243.6	03:43:43.36	−54:42:43.6	FIRE	dwarf
EUCL J034510.85−582115.9	03:45:10.85	−58:21:15.9	FIRE	dwarf
EUCL J035110.64−483806.7	03:51:10.64	−48:38:06.7	FIRE	dwarf?
EUCL J052656.21−545056.4	05:26:56.21	−54:50:56.4	FIRE	dwarf
EUCL J052929.24−461251.6	05:29:29.24	−46:12:51.6	FIRE	dwarf
EUCL J053001.69−523428.6	05:30:01.69	−52:34:28.6	FIRE	dwarf
EUCL J061759.55−492927.2	06:17:59.55	−49:29:27.2	FIRE	dwarf
EUCL J084714.14+641938.7	08:47:14.14	+64:19:38.7	KCWI; MOSFIRE	dwarf?
EUCL J091849.67+660353.1	09:18:49.67	+66:03:53.1	MOSFIRE	dwarf
EUCL J092049.59+711423.7	09:20:49.59	+71:14:23.7	KCWI	contaminant
EUCL J092540.76+693549.5	09:25:40.76	+69:35:49.5	KCWI	contaminant
EUCL J093005.83+720814.5	09:30:05.83	+72:08:14.5	KCWI; MOSFIRE	dwarf?
EUCL J094603.30+630522.1	09:46:03.30	+63:05:22.1	KCWI	dwarf?
EUCL J094617.98+652346.6	09:46:17.98	+65:23:46.6	KCWI	dwarf?
EUCL J100835.25+691935.8	10:08:35.25	+69:19:35.8	KCWI	dwarf
EUCL J102324.58+703158.6	10:23:24.58	+70:31:58.6	KCWI	dwarf?
EUCL J114858.03+743225.2	11:48:58.03	+74:32:25.2	LRIS	contaminant
EUCL J115159.14+682156.9	11:51:59.14	+68:21:56.9	KCWI	dwarf
EUCL J115853.41+683101.2	11:58:53.41	+68:31:01.2	KCWI	contaminant
EUCL J122605.56+731439.4	12:26:05.56	+73:14:39.4	KCWI	contaminant
EUCL J124115.79+662306.7	12:41:15.79	+66:23:06.7	KCWI	contaminant
EUCL J131224.33+670729.5	13:12:24.33	+67:07:29.5	LRIS	dwarf
EUCL J131809.35+700558.3	13:18:09.35	+70:05:58.3	KCWI	dwarf
EUCL J133810.37+685317.0	13:38:10.37	+68:53:17.0	LRIS	contaminant
EUCL J142441.75+693037.4	14:24:41.75	+69:30:37.4	KCWI	contaminant
EUCL J143351.31+540844.7	14:33:51.31	+54:08:44.7	MOSFIRE	contaminant
EUCL J144051.62+684954.5	14:40:51.62	+68:49:54.5	KCWI	contaminant
EUCL J144852.41+732435.6	14:48:52.41	+73:24:35.6	LRIS	contaminant
EUCL J154127.20+714353.1	15:41:27.20	+71:43:53.1	LRIS	dwarf?
EUCL J162903.17+683127.6	16:29:03.17	+68:31:27.6	MOSFIRE	contaminant
EUCL J170812.71+563448.0	17:08:12.71	+56:34:48.0	MOSFIRE	contaminant
EUCL J175348.34+665640.3	17:53:48.34	+66:56:40.3	LRIS	dwarf
EUCL J180128.23+651012.8	18:01:28.23	+65:10:12.8	LRIS	dwarf
EUCL J183032.83+585324.0	18:30:32.83	+58:53:24.0	MOSFIRE	dwarf
EUCL J215435.66+180214.9	21:54:35.66	+18:02:14.9	LRIS	dwarf